$K^+\Sigma(1385)$ Photoproduction at the BGOOD Experiment

Mrunmoy Jena

Masterarbeit in Physik
angefertigt im Physikalischen Institut

vorgelegt der
Mathematisch-Naturwissenschaftlichen Fakultät
der
Rheinischen Friedrich-Wilhelms-Universität
Bonn

April 2024

I hereby declare that this thesis was formulated by myself and that no sources or tools other than those cited were used.

Bonn, ...
Date Signature

1. Gutachter: Prof. Dr. Hartmut Schmieden
2. Gutachter: Prof. Dr. Ulrike Thoma

Acknowledgements

I am indebted to Prof. Dr. Hartmut Schmieden for introducing me to the exciting area of multiquark states and assigning this topic. I have benefited greatly from his insightful remarks and supervision. My special thanks goes to Dr. Tom Jude who guided me through many of the crucial steps in the analysis and for being always open for discussions, despite his busy schedule. Vlera and Emil, I am grateful to you both for volunteering to proofread my thesis and your valuable inputs all throughout. I thank Richard for being such a great office mate, our interesting conversations about physics and everything else kept me motivated. Finally, I am grateful to all other members of the BGOOD collaboration who have been extremely supportive throughout the duration of my thesis work.

Contents

CHAPTER 1

Introduction

1.1 Standard model

One of the most significant accomplishments of modern physics is the Standard Model, a well-tested, mathematical description of matter and its fundamental interactions as elementary particles. In this model, the elementary particles belong to two families: fermions, which obey Fermi-Dirac statistics and have half integer spins, and bosons, which follow Bose-Einstein statistics and have integer spins. The fundamental fermions are further grouped into two types: quarks (which take part in both strong and electroweak interactions) and leptons (which take part only in electroweak interactions). There are six flavours (three generations) of quarks and leptons, as shown in Fig. 1.1. The fundamental forces are

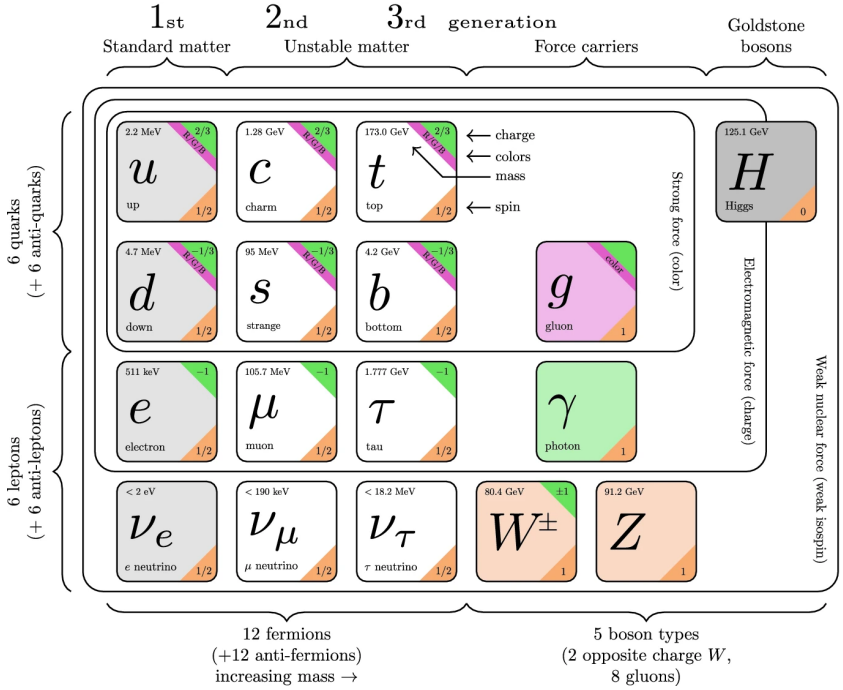

Figure 1.1: A schematic diagram of elementary particles in the Standard Model and their properties [1]

mediated by the vector (spin 1) bosons: the massive $W^{\pm}$ and Z^0 bosons mediating the weak interaction, gluons for the strong force and photons (γ) for the electromagnetic interaction. The massive bosons and fermions acquire mass by the Higgs mechanism: coupling to the Higgs field and spontaneous breaking of the electroweak symmetry [2]. The scalar (spin 0), massive Higgs boson is the excitation of this Higgs field.

Mathematically, the elementary particles can be seen as irreducible representations of the Poincaré group. The gauge fields coupling these particles arise as a result of making the corresponding Lagrangian invariant under local phase transformations [3]. The Standard Model is characterized by the gauge group:

$$SU(3)_C \otimes SU(2)_L \otimes U(1)_Y$$

The theory of strong interactions, Quantum Chromodynamics (QCD) is a gauge theory having $SU(3)_C$ symmetry, the C in the subscript denotes colour, which is a conserved quantity in this theory. A more detailed description of QCD is given in Section 1.3. The unified theory of electromagnetic and weak interactions (electroweak theory) is governed by the gauge symmetry $SU(2)_L \otimes U(1)_Y$. Here, the subscript L denotes weak isospin for left handed fermions and Y is the hypercharge [4].

1.2 Quark model

Following the discovery of a number of mesons and baryons in the 1950s and 60s, it was seen that the isospin multiplets could be classified based on their charge (Q), the third component of isospin (I_3), and the hypercharge ($Y = 2(Q - I_3)$). Murray Gell-Mann and Yuval Ne'eman independently developed an organizational scheme based on eight and ten dimensional representations of the approximate $SU(3)$ symmetry, called the 'Eightfold Way'. In the limiting case of exact SU(3) symmetry, the baryons and mesons would be seen as degenerate multiplets. On 'turning on' a symmetry breaking term in the Hamiltonian (i.e. making this term non zero), one obtains the isospin multiplets of the ordinary hadrons [5]. Notably, this classification was able to predict the quantum numbers and mass (through the Gell-Mann Okubo relation) of the Ω^- which was later discovered in 1964 [6].

A more fundamental explanation for the observed pattern of hadrons was found in the quark model (proposed by Gell-Mann and Zweig in 1964), which assumed that the light hadrons were bound states of fractionally charged constituents, 'quarks' (u,d,s): mesons formed out of a quark and an antiquark ($q\bar{q}$) and baryons as combinations of three quarks (qqq). The quarks belong to the fundamental triplet representation (**3**) and antiquarks to the antitriplet representation ($\bar{\mathbf{3}}$). A new internal degree of freedom, 'colour' was introduced to impose overall antisymmetry on the baryon wavefunctions, in accordance with Fermi statistics. All the hadrons are found to be colourless (colour singlet states), as a consequence of colour confinement (described in Section 1.3.2). The light meson and baryon multiplets are shown in Fig. 1.2.

The octet and singlet of light mesons arise naturally as a result of the flavour decomposition of the nonet formed from a quark-antiquark pair:

$$\mathbf{3} \otimes \bar{\mathbf{3}} = \mathbf{8} \oplus \mathbf{1}$$

Similarly, light baryons can be seen to arise from the following decomposition [7] (subscripts S, M, A

stand for symmetric, mixed-symmetric and anti-symmetric, respectively):

$$\mathbf{3} \otimes \mathbf{3} \otimes \mathbf{3} = \mathbf{10_S} \oplus \mathbf{8_M} \oplus \mathbf{8_M} \oplus \mathbf{1_A}$$

It is however to be noted that the singlet arising from the decomposition is not seen as a physical state due to the following symmetry considerations. The overall wavefunction needs to be antisymmetric under exchange of two quarks, the colour part, ϕ_{colour} is always antisymmetric and the spatial part for $l = 0$ baryons is symmetric. This means that the combined $\phi_{\text{flavour}} \times \phi_{\text{spin}}$ wavefunction must be symmetric. So an antisymmetric spin wavefunction is needed corresponding to the antisymmetric flavour wavefunction, however there is no antisymmetric ϕ_{spin} for a three quark system [3]).

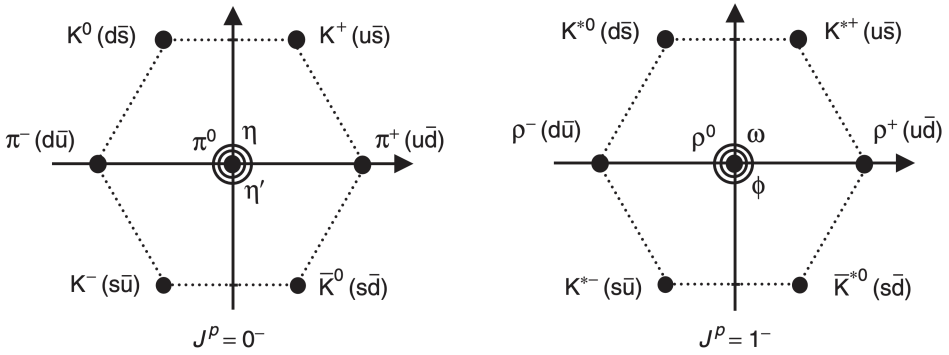

(a) Light mesons forming octets with $J^P = 0^-$ (pseudoscalar) and $J^P = 1^-$ (vector)

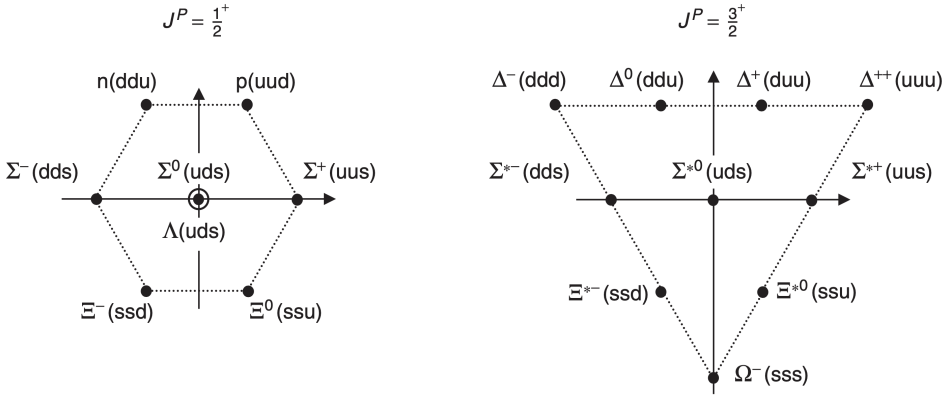

(b) Light baryons forming an octet with $J^P = \frac{1}{2}^+$ and decuplet with $J^P = \frac{3}{2}^+$

Figure 1.2: The geometrical arrangement of the light mesons and baryons, with the arrows indicating their quantum numbers (I_3, Y) (from [3])

1.3 Quantum chromodynamics

Following the successes of the quark model; a non-Abelian $SU(3)$ gauge theory, Quantum Chromodynamics emerged as a theory of strong interactions. The quarks can have either of the three colour states: r, g, b which form the fundamental triplet of $SU(3)_c$. Enforcing gauge invariance under local

$SU(3)_c$ transformations, leads to the introduction of eight coloured vector fields $A^a_\mu(x)$ $(a = 1 \dots 8)$ corresponding to eight gluons, analogous to the photon field in QED. The gluons thus form a colour octet, each carrying a colour charge and an anticolour. The QCD Lagrangian is given as:

$$\mathcal{L}_{QCD} = \psi(i(\partial_\mu - ig_s A^a_\mu T^a)\gamma^\mu - m)\bar{\psi} - \frac{1}{4}G^a_{\mu\nu}G^{a\mu\nu}$$

Here, the ψ are the spinors for the quark fields, g_s is the strong coupling constant, T^a are eight 3×3 matrices (generators of the $SU(3)$ group), γ^μ are the Dirac gamma matrices and m are the quark masses. The field strength tensor $G^a_{\mu\nu}$ is given by:

$$G^a_{\mu\nu} = \partial_\mu A^a_\nu - \partial_\nu A^a_\mu - g_s f^{abc} A^b_\mu A^c_\nu$$

The presence of the term linear in the structure constants (f^{abc}) in the expression of the field strength tensor $G^a_{\mu\nu}$ leads to gluon self interactions (three and four gluon couplings) in this theory. This is in turn a consequence of QCD being non Abelian (i.e. the generators do not commute, $[T^a, T^b] = if^{abc}T^c$). As a result of the gluons being self interacting and carrying colour charge, two interesting features emerge in QCD: asymptotic freedom and colour confinement [2].

1.3.1 Asymptotic freedom

In order to absorb UV divergences in the theory and thereby produce finite results for physical quantities, the QCD coupling constant ($\alpha_s = g_s^2/4\pi$) is redefined (or 'renormalized') as a function of an arbitrary renormalization scale, μ_R . Usually the renormalization scale is chosen to be close to the momentum transfer ($\mu_R \approx Q$), and as such $\alpha_s(\mu_R^2)$ corresponds to the effective strength of the interaction. The renormalized coupling constant is obtained by solving the following Renormalization Group equation:

$$\mu_R^2 \frac{d\alpha_s}{d\mu_R^2} = \beta(\alpha_s^2) = -(b_0\alpha_s^2 + \cdots)$$

where $b_0 = (33 - 2n_f)/(12\pi)$ is the 1-loop coefficient of the β function. The "running" of $\alpha_s(\mu_R^2)$ is then given as (at the lowest order) [4]:

$$\alpha_s(\mu_R^2) = \frac{1}{b_0 \log\left(\frac{\mu_R^2}{\Lambda_{QCD}^2}\right)}$$

The positive value of b_0 and hence the negative β function in QCD leads to the theory being 'asymptotically free', meaning that the effective coupling is quite strong at low energies (or equivalently large distances) and becomes weak at high energies. As such for energies above the QCD scale parameter Λ_{QCD} ($\approx 332 \pm 17$ MeV for 3 quark flavours [8]), perturbative techniques may be applied, which is however not possible at energies below this scale parameter. A plot of the QCD running coupling constant is shown in Fig. 1.3

Physically, the negative β function and hence asymptotic freedom can be understood to arise from the fact that the gluons in QCD are self-interacting unlike the photon in QED. In QED, the electromagnetic field in the vacuum can produce electron-positron pairs (vacuum polarisation) which leads to a 'screening'

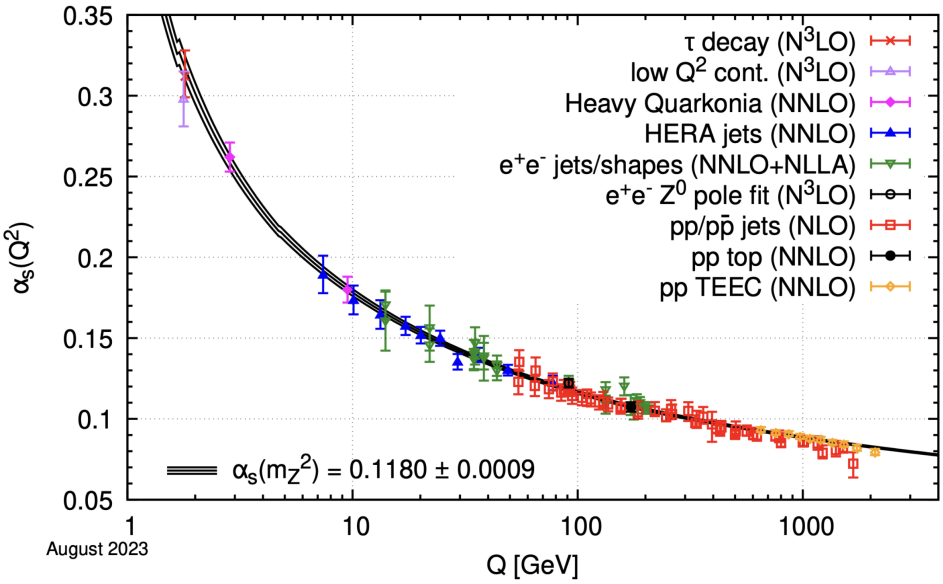

Figure 1.3: The running coupling $\alpha_s(Q^2)$ determined from different measurements compared with QCD predictions (solid curve) (from [7])

of the effective electric charge (decrease with increasing distance). An analogous screening of colour charge takes place in QCD, through $q\bar{q}$ loops. However, the gluonic self interactions produce an opposite 'antiscreening' of the colour charge and it is seen these contributions dominate over the screening effect, thereby leading to this atypical behaviour of the strong coupling constant.

1.3.2 Colour confinement

As outlined before, the coloured quarks and gluons have never been observed to be free and are instead bound inside these colour singlet hadrons. Although an analytical proof of colour confinement has not yet been found, some phenomenological non-relativistic (for heavy quarks) $q\bar{q}$ and qqq potentials have been proposed, which in fact show good agreement with the spectra of $c\bar{c}$ and $b\bar{b}$ mesons. One of the often cited ones is the Cornell potential (shown here for $q\bar{q}$):

$$V(\vec{r}) = -\frac{4}{3}\frac{\alpha_s}{r} + \sigma r$$

This form of the inter-quark potential is shown in Fig. 1.4. Here, the first term $V_{Coulomb}(r) \propto -1/r$ is a Coloumb-like attractive potential, relevant for short distances (in the regime of asymptotic freedom). Analogous to QED, this term arises from the exchange of one massless gluon. The factor of $4/3$ is the colour factor for a $q\bar{q}$ interaction mediated via gluon exchange. The second term, $V_{conf} \propto r$, is the linear confinement potential with a constant $\sigma \approx 0.89$ GeV/fm called the 'gluon string tension' [10]. This part of the potential is responsible for the long range interaction. Due to the self interaction of the gluons, the colour field between two (approximately) static quarks gets effectively squeezed into a one dimensional 'flux tube' or 'string'. From the form of the potential it is clear that the energy stored in this gluon field increases with the inter-quark separation, as such it would take an infinite amount of energy to free the

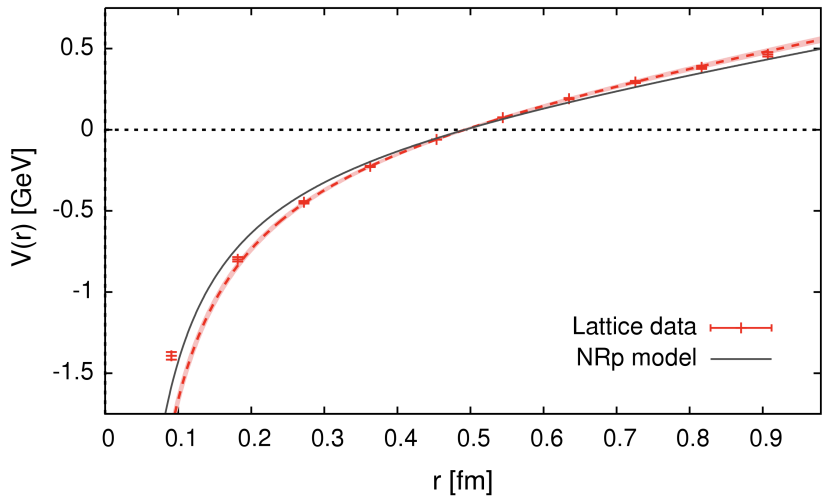

Figure 1.4: Interquark potential for a $c\bar{c}$ system, lattice QCD result compared with a non relativistic potential (NRp) model (from [9])

$q\bar{q}$ pair. Instead, when the momentum transfer to this system is large enough, new mesons or baryons are produced (known as hadronization) which may subsequently be seen as collimated jets in particle detectors, for example [3, 11].

1.4 Exotic hadrons

While the ordinary hadronic states are categorized into baryons (qqq) and mesons ($q\bar{q}$), the rich theory of strong interactions does not forbid the existence of other unconventional structures. In fact, in the very papers that introduced the quark model, Gell-Mann and Zweig had both proposed that multi-quark configurations such as: $qq\bar{q}\bar{q}, qqqq\bar{q}, qqqqq\bar{q}\bar{q}\cdots$ are possible [12, 13]. The inclusion of gluons into this picture in QCD further extends the allowed configurations to include hybrid baryons ($qqqG, \cdots$), hybrid mesons ($q\bar{q}G, \cdots$), glueballs ($GG, GGG, \cdots$), etc. [10]

Some sources group these predicted states into: spin exotic (configurations with J^{PC} quantum numbers that are not allowed for ordinary hadrons), flavour exotic (with unusual combinations of isospin and strangeness) and crypto exotic states (having the usual quantum numbers but with properties that can't be explained by quark models) [6, 14]. The field of hadron spectroscopy is therefore quite interesting and provides valuable insights into properties of low energy QCD (i.e. in the confinement regime).

1.4.1 Theory and phenomenological models

A number of theoretical and phenomenological models have been proposed to understand exotic hadrons and their properties. A prominent picture that often comes up is that of a compact multiquark state, i.e. an exotic state in which four or more quarks are bound tightly, interacting via attractive one-gluon exchange. In this model, two or more 'coloured' subclusters - diquarks or diantiquarks combine together to form colour neutral states. From the $SU(3)$ colour algebra, it can be seen that the direct product of

two colour triplets (**3**) gives an antisymmetric antitriplet ($\bar{\mathbf{3}}_\mathbf{A}$) and a symmetric sextet ($\mathbf{6}_\mathbf{S}$):

$$\mathbf{3} \otimes \mathbf{3} = \bar{\mathbf{3}}_\mathbf{A} \oplus \mathbf{6}_\mathbf{S}$$

On taking products of the corresponding $SU(3)$ matrices, one finds that the term for the $\bar{\mathbf{3}}_\mathbf{A}$ representation has a negative coefficient indicating an attractive interaction and the coefficient for the $\mathbf{6}_\mathbf{S}$ representation is positive, indicating repulsion. As such, in most phenomenological studies the sextet is dropped and the diquark $[qq]$ is taken as a colour antitriplet and equivalently a diantiquark $[\bar{q}\bar{q}]$ as a colour triplet. Further, the two quarks (each with spin-1/2) could combine with anti-parallel spins, forming a spin-0 diquark or have a parallel spin alignment, resulting in a spin-1 diquark. The former is called a 'good diquark' as it can be bound strongly and the latter a 'bad diquark' which is less tightly bound, on account of Pauli repulsion [15].

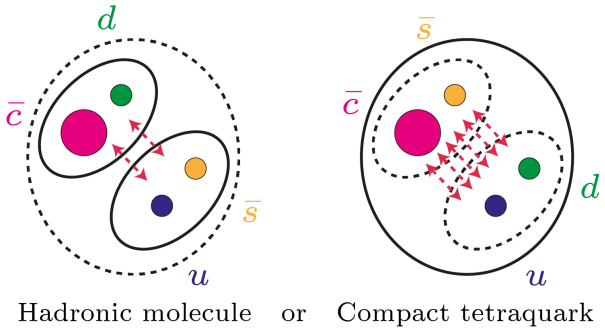

Figure 1.5: Comparison between the two prominent models for exotic hadrons (from [16]). In the hadronic molecular picture, the dotted lines indicate meson exchange, while for the compact tetraquark they indicate gluon exchanges.

The other manner in which the exotics could be seen is in the form of hadronic molecules. In these systems, meson exchanges generate an attractive molecular force, holding together the meson-meson (tetraquark) and meson-baryon (pentaquark) states. This model seems to be of widespread interest, as it can partly account for the closeness of the exotic resonances to two particle thresholds. The binding energy of such a state is then just the difference between the sum of the masses of the two constituent hadrons (two mesons for a tetraquark or a meson and a baryon for a pentaquark state) and the mass of the exotic two-hadron system:

$$E_b = m_1 + m_2 - M_{exotic}$$

with a corresponding momentum scale: $\gamma = \sqrt{2\mu E_b}$ with μ being the reduced mass of the system. By application of the uncertainty principle, a small binding energy gives a large hadronic radius for this molecule ($r \approx 1/\gamma$), and as such these exotics are interpreted as loosely bound, extended objects [15, 17].

Another model is that of hybrids (such as $q\bar{q}G$), where the gluon flux tube between the quarks is in an excited state, leading to new degrees of freedom in addition to the usual radial and rotational excitations that the quarks or antiquarks possess in ordinary hadrons. As such these models could explain states having exotic quantum numbers (for example mesons with $J^{PC} = 0^{--}, 0^{+-}, 1^{-+}$ etc. that can't arise from a simple $q\bar{q}$ pair) [18, 19]. Hadroquarkonia states are also discussed in which a heavy colour singlet state (such as $c\bar{c}$) is embedded in an extended cloud of light quarks and/or gluons; the interactions between this cloud and the heavy 'core' occurring through a QCD Van der Waals like force, similar to the molecular picture [20].

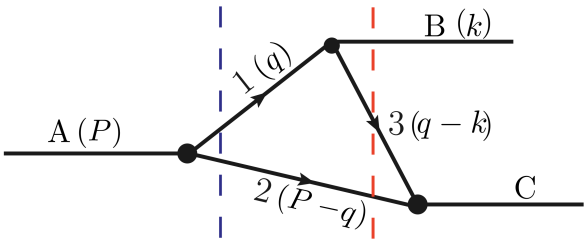

Figure 1.6: Triangle diagram for $A \rightarrow B + C$ (dashed lines indicate cuts defined in [21])

While it is alluring to identify narrow peaks seen in the invariant mass distributions of final state hadrons as resonances; *Guo et. al.* [21] remark that these peaks may, in some cases be caused due to other kinematical effects. Their study defines genuine resonances as 'dynamical poles' in the S matrix (transition amplitude), i.e. the positions of these poles is dependent on the strength of the hadronic or quark level interactions. On the other hand, 'kinematical singularities' in the S matrix, such as in triangle diagrams occur simply due to the intermediate particles becoming on-shell (i.e. obeying energy-momentum relation: $p_i^2 = m_i^2$) and are not related to resonances. Fig. 1.6 for example, shows the process $A \rightarrow B + C$ proceeding through decays to intermediate states 1, 2 and 3. Since these are on shell, they can be interpreted as real particles propagating in time. In certain cases, a 'cusp-like' structure in the differential cross sections near thresholds might be driven by contributions from both true exotic resonances and triangle singularities. Moreover the lineshapes for the former may be distorted due to varied couplings to multiple channels and from interference caused by backgrounds. Therefore, the interpretation of unconventional hadronic states can be quite challenging.

1.4.2 Experimental evidence of multiquark states

Although predictions for exotic hadrons had been around since the 1960s, experiments did not provide any conclusive evidence of these states for many decades. However, this changed in 2003, when the very first non-standard hadron, the $X(3872)$ was discovered unexpectedly by the BELLE experiment. It was seen as a narrow peak in the invariant mass distribution of $\pi^+\pi^- J/\psi$, for the decay: $B^\pm \rightarrow K^\pm(\pi^+\pi^- J/\psi)$, shown in Fig. 1.7. Subsequent confirmations came from the BABAR (in e^+e^- collisions), CDF and D0 (in $p\bar{p}$ collisions) and also the LCHb (pp collisions) [17]. The current average value for its mass is 3871.69 $\pm$ 0.17 MeV with an extremely narrow width of 1.2 MeV and quantum numbers $J^{PC} = 1^{++}$. Its mass does not match with the constituent quark model predictions for masses of low lying $J = 1^{++}$ charmonium states [22]. Furthermore, the observation of the decay mode $X(3872) \rightarrow J/\psi\rho^0(\rho^0 \rightarrow \pi^+\pi^-)$ suggests a significant isospin violation, in case the $X(3872)$ is regarded as a simple $c\bar{c}$ pair. As such this state is interpreted to have an extended quark configuration of $c\bar{c}u\bar{u}$ [23]. The fact that this state resides very close to the $D^0\bar{D}^{*0}$ threshold lends credence to a $D^0 - \bar{D}^{*0}$ molecular interpretation, although the exact structure for this exotic state is still debatable. Following this discovery, a number of heavy tetraquark candidates (collectively called the XYZ states) have been found both in the charm and bottom sector.

In the case of exotic heavy baryons, compelling evidence for the presence of pentaquark states was found in 2015 in the analysis of the $\Lambda_b^0 \rightarrow J/\psi p K^-$ ($J/\psi \rightarrow \mu^+\mu^-$) decay at the LHCb (Run 1). A significant peak was seen in the $J/\psi p$ mass distribution which could not be accounted for, just by the contributions coming from the $\Lambda^* \rightarrow pK^-$ decays. To produce good fits to this mass distribution, two exotic pentaquark structures (with a minimal quark content of $uudc\bar{c}$) were additionally needed: a narrow

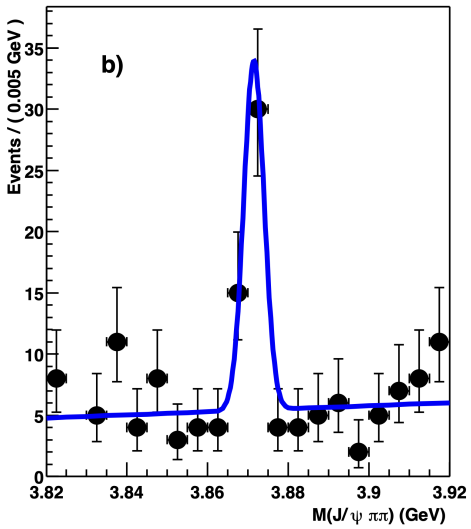

Figure 1.7: The $X(3872)$ seen as a narrow peak in the $M(\pi^+\pi^- J/\psi)$ distribution (from [24])

$P_c(4450)^+$ ($\Gamma = 39 \pm 20$ MeV) and a broader $P_c(4380)^+$ (205 ± 88 MeV). A much larger dataset was analyzed in 2019 (including the Run 2 data). An additional narrow exotic $P_c(4312)^+$ resonance showed up, along with the observation that the previously seen single peak at 4450 MeV resolves into two peaks at 4440 and 4457 MeV, as shown in Fig. 1.8. However, the updated analysis neither confirms nor rules out the presence of the $P_c(4380)^+$ state [7]. Similar to the observations in the meson sector, these P_c states are found to be in close proximity to $\Sigma_c^{(*)}\bar{D}^{(*)}$ mass thresholds, hinting at an interpretation of these states as meson-baryon molecules. It is noteworthy to mention that recently, a charmed strange pentaquark $P_{cs}(4338)^0$ (with minimal quark content of $c\bar{c}uds$) has been found by the LHCb in the decay $B^- \to J/\psi\Lambda\bar{p}$, at a high statistical significance ($> 14\sigma$). It again seems to be consistent with the molecular picture, with its mass being just at the $\Xi_c\bar{D}$ threshold, along with a narrow width [25].

1.5 Motivation for the present study

In analogy to the exotic hadrons found in the heavy charm and bottom sectors, quite interesting observations have also been been made in the light uds sector. Notably, similar to the theoretical model used to predict the P_c states at LHCb, a dynamically generated vector meson-baryon resonance in the strange sector (the $N^*(2030)$) was used to describe a cusp like structure seen (at the K^* threshold) in the differential cross section of the process $\gamma p \to K^0\Sigma^+$. This state was found to enhance the destructive interference between the $K^*\Lambda$ and $K^*\Sigma$ intermediate states, leading to a decrease in the differential cross section [27]. On a similar note, this interference was predicted to be constructive in the channel $\gamma n \to K^0\Sigma^0$, thereby producing an enhancement in its differential cross section. Experimental results for this channel at the BGOOD experiment show a peak in the differential cross section with a shape and position falling in line with the prediction. Interestingly, the same molecular type $N^*(2030)$ is seen to also drive a triangle singularity process for the photoproduction of the $K^+\Lambda(1405)$ on a proton target, leading to a cusp in its differential cross section around 1900 MeV [28, 29].

Recently, measurement of the differential cross section for $\gamma p \to K^+\Sigma^0$ taken at forward angles

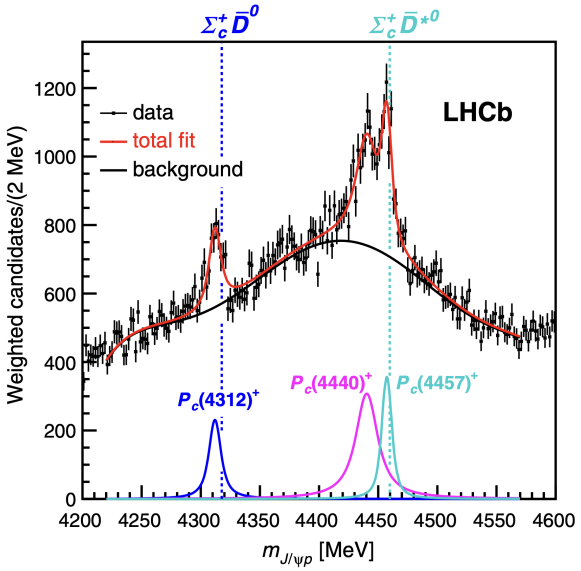

Figure 1.8: The LHCb pentaquark states identified in the 2019 analysis. The baryon-meson $\Sigma_c \bar{D}^{(*)}$ thresholds are indicated by the dotted lines (from [26])

($\cos\theta^K_{CM} > 0.9$), showed a cusp again around 1900 MeV. When extrapolated to minimum momentum transfer (t_{min}) and to $\cos\theta^K_{CM} = 1$, the differential cross section ($d\sigma/dt$) showed an even steeper downfall by 75 % at this centre of mass energy. This peculiar structure along with its closeness to a number of strange hadronic thresholds, led the authors to speculate that this structure could be driven by yet another exotic molecular state in the strange sector [30]. One such driving mechanism could be a narrow bound state of the $K^+\Sigma(1385)$, which is proposed by *Huang et.al.* [31] to have a mass of 1872.6 MeV and a binding energy of 7.4 MeV, with quantum numbers $I(J^P) = \frac{1}{2}(\frac{3}{2}^-)$. The quantum numbers of this exotic state are also found to be the same as that of the nucleon resonance $N^*(1875)$. Moreover, such a molecular state in the strange sector strikes parallels to the $P_c(4380)$ pentaquark in the charm sector, which has in turn been interpreted as a $\Sigma_c^* D$ molecule with the same $I(J^P)$ quantum numbers. If such an exotic state indeed exists, a measurement of the differential cross section for $\gamma p \rightarrow K^+\Sigma^*$ would show a rise and a peak like structure beyond its production threshold.

It is however noted that the latest measurement (from the CLAS collaboration) of the differential cross section for this process was taken at energies above threshold (starting at 2 GeV) and at relatively backward angles ($-0.85 < \cos\theta^{K^+}_{\mathrm{CM}} < 0.84$). As such, the current study gives the very first measurement of the differential cross section for $\gamma p \rightarrow K^+\Sigma(1385)$ photoproduction, at very forward angles ($0.9 < \cos\theta^{K^+}_{CM} < 1.0$), and around the threshold region, in order to study whether the $K^+\Sigma(1385)$ final state shows any interesting near-threshold behaviour. The study also aims to provide a physical interpretation to measured differential cross section for this process. The measurement presented here is based on the dataset collected in a beam time in April-May 2017, which used a short (effective length of 6.1 cm), liquid hydrogen target.

CHAPTER 2

Experimental Setup

The BGOOD experiment at the University of Bonn is a fixed target photoproduction experiment well suited to provide insights into physics in two main areas, namely exotic hadronic states in the light quark (*uds*) sector and coherent photoproduction of mesons off the deuteron. Essential to the operation of this experiment is the Electron Stretcher Accelerator (ELSA), which provides accelerated electron beams of energies up to 3.2 GeV. The ELSA is described in Section 2.1 and the details of the experimental setup of the BGOOD are given in Section 2.2.

2.1 ELSA facility

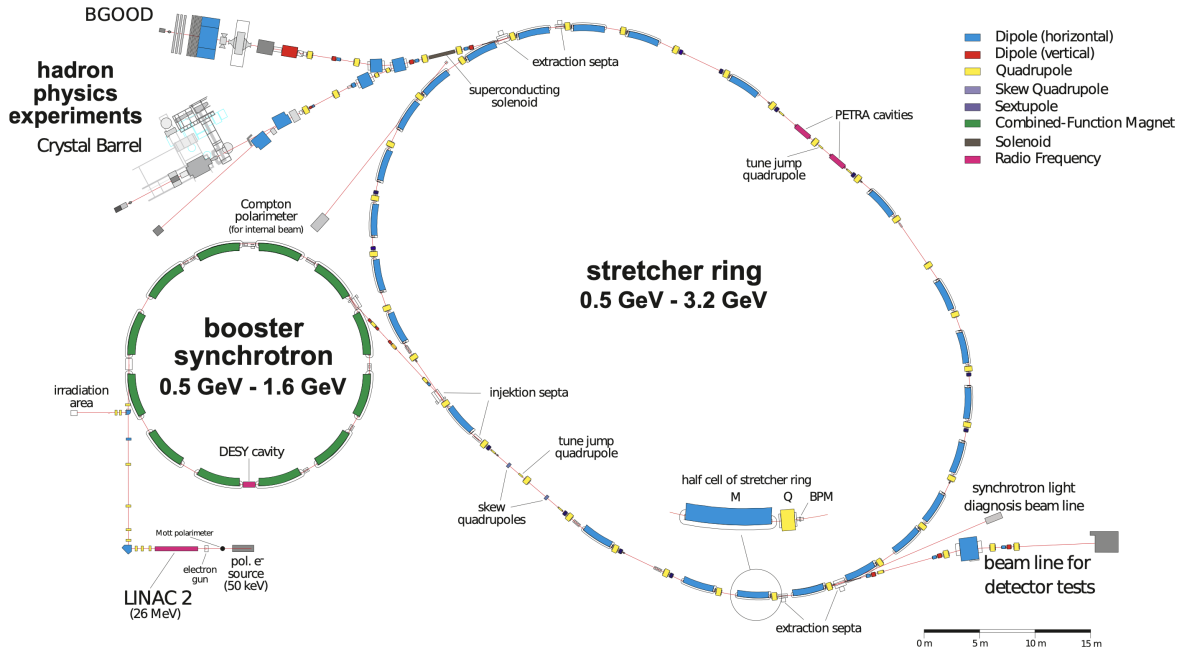

Figure 2.1: A schematic diagram of the Electron Stretcher Accelerator (from [32])

Situated beneath the Physics Institute at the University of Bonn, the Electron Stretcher Accelerator (ELSA) is composed of three stages. In the first stage, a thermal electron gun removes electrons from a cathode material and these electrons are subsequently fed into a linear accelerator LINAC which accelerates them to an energy of 26 MeV. In the second stage, the electron beam is injected into a booster synchrotron running at a frequency of 50 Hz, which further accelerates the beam up to 0.5 to 1.6 GeV. Once the required energy is attained, the beam is extracted and enters the third stage, the stretcher ring. A number of injections of the electrons into the stretcher ring (separated by 2 ns) take place, until this ring is homogeneously filled. This is followed up by further accelerating the electron beam up to the required energy (a maximum of 3.2 GeV). Once this has been achieved, the final electron beam is diverted either to a facility for detector tests or to one of the two hadron physics experiments: BGOOD and the Crystal Barrel [32]. A schematic for ELSA is shown in Fig. 2.1.

2.2 BGOOD experiment

The BGOOD experiment is designed in such a manner that it is able to investigate very low momentum transfer dynamics, which results in the final state mesons going at forward angles. The remaining excited hadronic system is therefore nearly at rest and its decay products cover the full solid angle. In order to detect these decay products, the central detector covering polar angles: $25° < \theta < 155°$, is ideal. Angles less than 25° (forward angles) are covered by the intermediate and forward detectors. Fig. 2.2 provides an overview of various components of the BGOOD experiment. The following subsections include descriptions of the production of photon beams and tagging (Section 2.2.1), the target (Section 2.2.2), components of the central detector (Section 2.2.3), the intermediate detector - SciRi (Section 2.2.4), the forward spectrometer for detecting forward going mesons (Section 2.2.5) and finally readout of the photon flux (Section 2.2.6) at the end of the experiment.

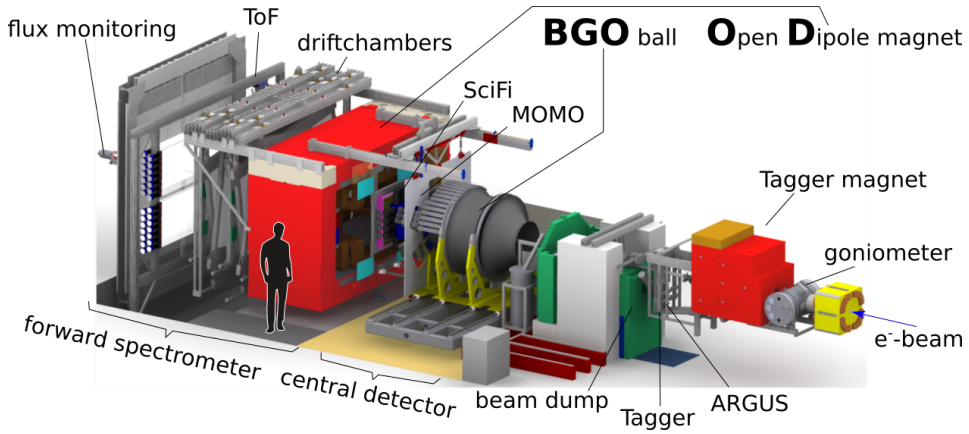

Figure 2.2: An illustration showing the design and components of the BGOOD experiment (from [32])

2.2.1 Generation of photon beam and photon tagging

In order to produce the photon beam for this experiment, the electron beam available from the ELSA is made to impinge on a radiator and then undergoes the bremsstrahlung process. The goniometer

tank consists of these radiators mounted on a wheel, which can be rotated to align them with the incoming electron beam. Copper radiators are used for producing unpolarized photons via incoherent bremsstrahlung, while a diamond radiator is used for the production of linearly polarized photon beams through coherent bremsstrahlung (here the entire crystal lattice takes up the recoil momentum). The photon beam produced from both these methods has a continuous energy spectrum and measuring this energy is important, which is where the tagger system comes in. The produced photon beam and post bremsstrahlung electrons pass into the magnetic field of the tagger dipole magnet. While the photon beam passes through unaffected, the trajectory of the post bremsstrahlung electrons is curved (determined by the Lorentz force equation). A hodoscope, which consists of 120 plastic scintillators precisely determines the energy of post bremsstrahlung electrons (E). This can be subtracted from the known intial electron beam energy (E_0) to give the tagged photon beam energy (E_γ):

$$E_\gamma = E_0 - E$$

Electrons that do not participate in the bremsstrahlung process are stopped in the beam dump and their energy is not determined by the tagging hodoscope [32, 33]. A schematic view of the tagger system is shown in Fig. 2.3.

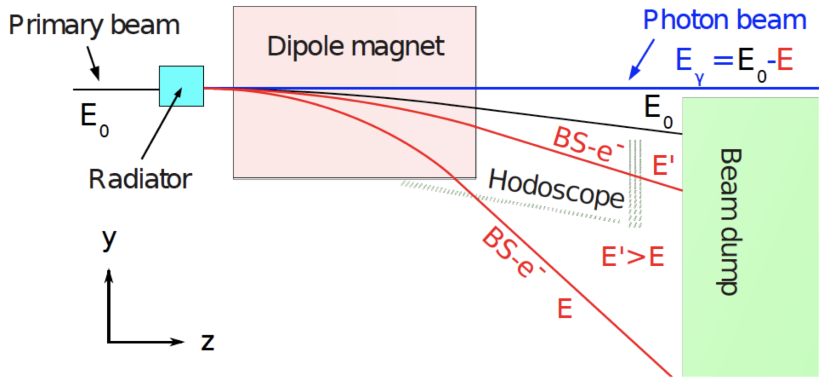

Figure 2.3: A diagram showing the working principle of the tagger at the BGOOD experiment (from [32]). The solid black curve indicates the electrons that do not undergo bremsstrahlung, thereby retaining their original energy (E_0), and pass directly into the beam dump. Red solid curves indicate the bremsstrahlung electrons, with final energies E' and E. The post bremsstrahlung electron beam with lower energy (E) is bent more in the magnetic field.

2.2.2 Target

For the experiment, the target (placed in the central part of the BGO Ball) can be either a solid state material such as carbon, or may be a cryogenic liquid (hydrogen or deuterium). The target cell for the cryogenic liquids is a hollow cylinder made up of aluminium. It has thin Mylar foil windows on either side to allow for the entry and exit of the photon beam. The cryogenic target cell which is either 5 cm or 10 cm long is placed inside a vacuum pipe; due to the pressure difference it expands and the effective length becomes 6.1 cm or 11.1 cm respectively [34]. For the present work, data is taken using a liquid hydrogen target with effective length of 6.1 cm for April/May 2017 runtime.

2.2.3 Central detectors

The central detector system surrounds the target cell, and is composed of various detectors: two cylindrical Multi-Wire Proportional Chambers (MWPCs), a plastic scintillating barrel and the BGO Ruby ball.

The two gas filled MWPCs consist of anode wires which run parallel to the beam direction and two cathode strips wound helically in opposite directions (±45°) around the anode wires. The arrangement allows these MWPCs to reconstruct charged particle tracks close to the target and to determine displaced reaction vertices.

The scintillator barrel is segmented into 32 plastic bars, each being 5 mm thick, arranged together in the form of a cylinder. This detector is used to find energy loss ($\Delta E/\Delta x$) of charged particles. As it responds to only charged particles while the BGO Ball does so for both charged and neutral particles; signals from the scintillator barrel can be used in combination with those from the BGO Ball to tell apart tracks of charged and uncharged particles.

The outermost part of the central region, the BGO Ruby Ball is composed of 480 Bismuth Germanate ($Bi_4Ge_3O_{12}$) crystals, with 15 sectors of these, each of which has 32 crystals. The reason for the choice of this inorganic material is that it has a small radiation length and offers sufficient energy resolution. The complete arrangement covers the central region in polar angle, $\theta \in [25, 155]°$. Each crystal covers a polar angular element $\Delta\theta$ from $6 - 10°$ and $\Delta\phi = 11.25°$ in the azimuthal angle. In the present work, this detector is used to determine the position and energy of photons. These produce electromagnetic showers (via Compton scattering, photoelectric effect and pair production) in the calorimeter and their entire energy is absorbed by the BGO crystals. The readout of the signal can be done from Photomultiplier Tubes (PMTs) which are connected to each of these crystals [33]. Fig. 2.4 shows the central detector of the BGOOD experiment along with various components in this region.

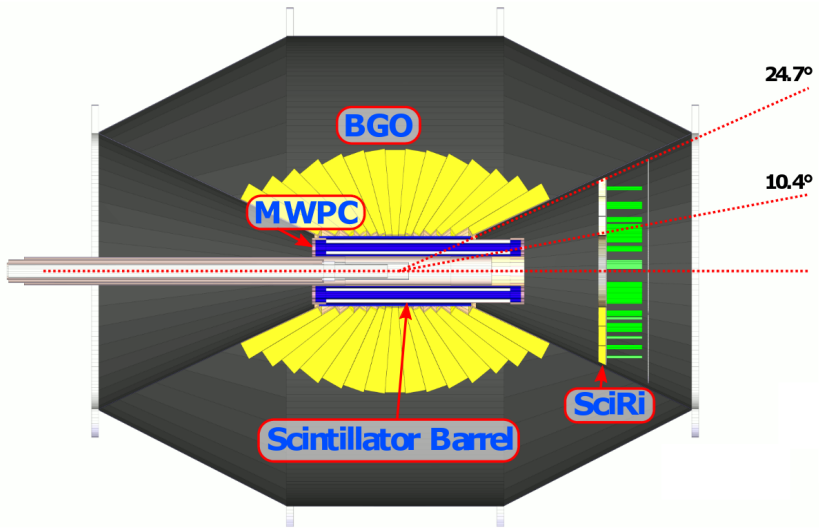

Figure 2.4: The central detector of the BGOOD experiment. The intermediate detector SciRi is also shown here. (from [34])

2.2.4 Intermediate detector - SciRi

The scintillating ring (SciRi) detector provides angular coverage ($\theta \in [10, 25]°$) over the gap between the central region covered by the BGO and the forward angle acceptance of the forward detector; with partial overlap with the coverage of the MWPCs and the scintillator barrel. This detector is composed of three rings, each of which is 20 mm thick and is made up of 32 plastic scintillators. Each ring has a polar and azimuthal acceptance of $\Delta\theta = 5°$ and $\Delta\phi = 11.5°$ respectively. This detector aids in identification of charged particles. Signal readout is done via avalanche photodiodes [32].

2.2.5 Forward spectrometer

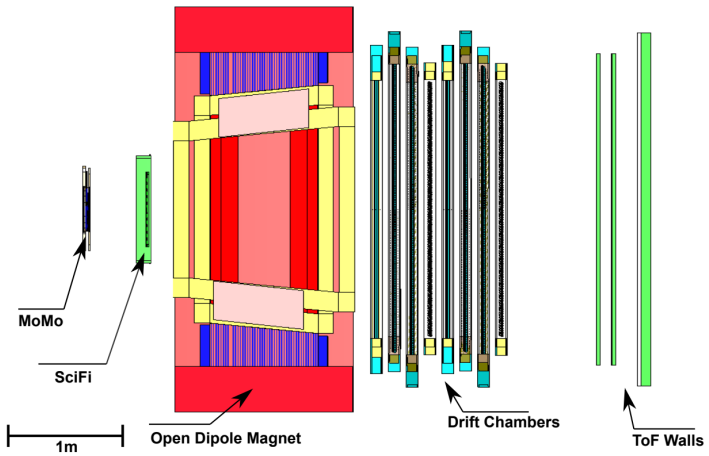

Figure 2.5: Components of the Forward Spectrometer in the BGOOD experiment (from [35])

The forward spectrometer is one of the most important parts of the BGOOD experiment, which serves the purpose of full identification of forward going particles ($\theta < 10°$) by combining measurement of the three momentum (by reconstructing trajectories) along with the velocity of these particles. This is done by tracking detectors which determine the particle trajectories, placed before (upstream) and after (downstream) an open dipole magnet. Time of flight (ToF) walls at the end of the forward spectrometer record the timing information.

In more detail, MOMO and SciFi are the two scintillating fibre detectors placed upstream of the open dipole magnet. The MOMO consists of three layers of a total of 672 fibres, with consecutive layers having an angle of 60° between them. The SciFi detector is rectangular in shape, with 640 fibres which are arranged perpendicular to each other. Combined information from the layers of these detectors determine the trajectory of the particles before entering the magnetic field. The readout is taken using photomultiplier tubes (PMTs). Both detectors have a small hole/window in the center to allow for passage of photons which do not interact with the target.

A heavy open dipole (OD) magnet generates a magnetic field allowing for the momentum and charge determination of charged particles. Usually a 'half field setting' of 0.216 T is used during data acquisition, i.e. the field is set to half of the maximum value. This is done so that the charged particles carrying low energy can still be detected (albeit with lower momentum resolution), which would otherwise bend out of the acceptance region of the detectors downstream of the magnet, if a higher magnetic field is applied.

A maximum achievable integrated magnetic field strength of 0.71 Tm is achievable at 1340 A.

Beyond the dipole magnet, an arrangement of 8 drift chambers is placed, which have four different wire orientations: H (vertical), Y (horizontal), U and V (rotated by ±9° respectively against the vertical). The naming is with respect to a plane normal to the beam axis. Further these drift chambers are each built out of two layers of hexagonal cells. These drift chambers together allow for the determination of the trajectory of particles downstream of magnet.

At the very end of the forward spectrometer are the three ToF walls, made out of plastic scintillators oriented horizontally. Signal readout is again done with PMTs coupled to these ToF walls at both ends. This gives the horizontal hit position. The vertical position of the hit is given by the bar position itself. Time of the hits in the ToF walls acts as a stop signal, the start signal being given by the tagger. Subtracting the tagger to target travel time for the photon beam from the difference between the start and stop signals gives the time of flight (from target to the ToF walls) of the particles. From this information and the known distance travelled, the relativistic velocity β of the particles can be calculated [35, 36].

2.2.6 Measurement of photon flux

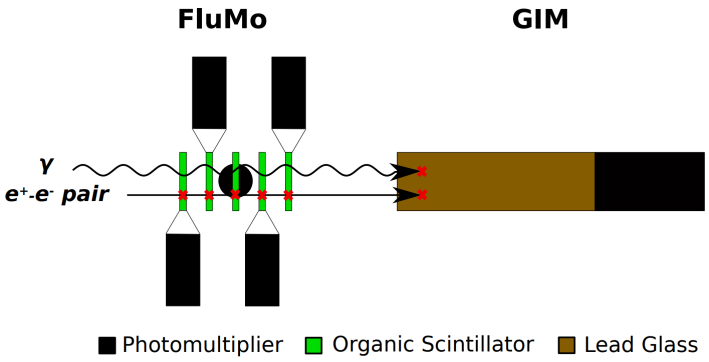

Figure 2.6: Schematic showing the photon flux monitors FluMo and GIM. Since the FluMo doesn't directly detect the photons, interactions (red crosses) are not shown for photon beam for this detector. [33])

At the very end of the experimental setup, two detectors are placed (more than 7 m downstream from target) for the measurement of the incident photon flux: Flux Intensity Monitor (FluMo) and Gamma Intensity Monitor (GIM). The monitoring of photon flux is required for the normalization of the differential cross section. The two flux monitors are shown in Fig. 2.6.

The GIM is made of lead glass and completely absorbs the incident photons. The photons produce electromagnetic showers in the material which subsequently give out Cherenkov radiation. This signal is read out by a PMT. As it has almost 100 % photon detection efficiency, it can record the absolute photon flux. This is however used only at low beam intensities in order to prevent radiation damage and circumvent saturation from dead time effects.

For high beam intensities while taking data, the FluMo detector is used. It consists of five plastic scintillators and indirect measurement of the photon flux can be done by measuring the number of e^+e^- pairs produced (pair production process: $\gamma \rightarrow e^+e^-$). Since only a fraction of the incoming photons undergo pair production process, combining this measurement with the absolute flux determined by the GIM (at low intensities) gives the fraction of flux measured by the FluMo. From this ratio, the actual photon flux during data taking can be calculated [32].

CHAPTER 3

Analysis

As a first step in the analysis of data from the BGOOD experiment, the ExPLORA framework is used. This goes all the way from decoding and calibration of the raw data to forming clusters from the hit information from detectors and reconstructing tracks of different particles, giving the user meaningful data to analyse. Moreover, ExPLORA was also used to generate Monte Carlo simulations for specific reactions, using an event generator and simulating the decays of the final state particles and their subsequent passage through matter. This is outlined in Section 3.1 [35].

The reaction of interest for the present work is the photoproduction process $\gamma p \rightarrow K^+\Sigma(1385)$ at very forward angles ($0.9 < \cos\theta^{K^+}_{CM} < 1.0$). The differential cross section calculation for this process is done by using two reconstructed missing mass distributions: missing mass from a K^+ and two π^0's (MM($K^+\pi^0\pi^0$)), and missing mass from a K^+ and a single π^0 (MM($K^+\pi^0$)). The steps starting from the generation of simulated data till the calculation of the differential cross section are detailed in Sections 3.2 to 3.8.

3.1 Analysis framework

3.1.1 ExPLORA

The **Ex**tended **P**luggable **O**bjectoriented **R**OOTified **A**nalysis (ExPLORA) framework was initially implemented for the CBELSA/TAPS experiment, and subsequently, a reduced version has been used as the primary tool for analysis at the BGOOD experiment. This framework is written in C++ and extends the functionality of the ROOT library. The complete analysis chain in this framework is formed out of configurable 'plugins' which are algorithms dedicated to an individual task in the analysis (such as say, a clustering algorithm) and 'containers' which encapsulate some physics information (for example, a container for clusters of hits), facilitating exchange of data between the plugins [37]. Additionally, XML (e**X**tensible **M**arkup **L**anguage) is used to provide a structural description to the framework. An overview of the structure of ExPLORA is shown in Fig. 3.1.

The first stage in the process involves readout of raw data from the detectors, combining them to form a single event and storing this information on disk. The analysis software then decodes this raw data, followed by mapping the raw channel numbers onto detector channels, along with applying timing corrections and calibration factors from a database. Data collected from various readout modules which belong to one detector, is grouped together. In the reconstruction process, additional information about

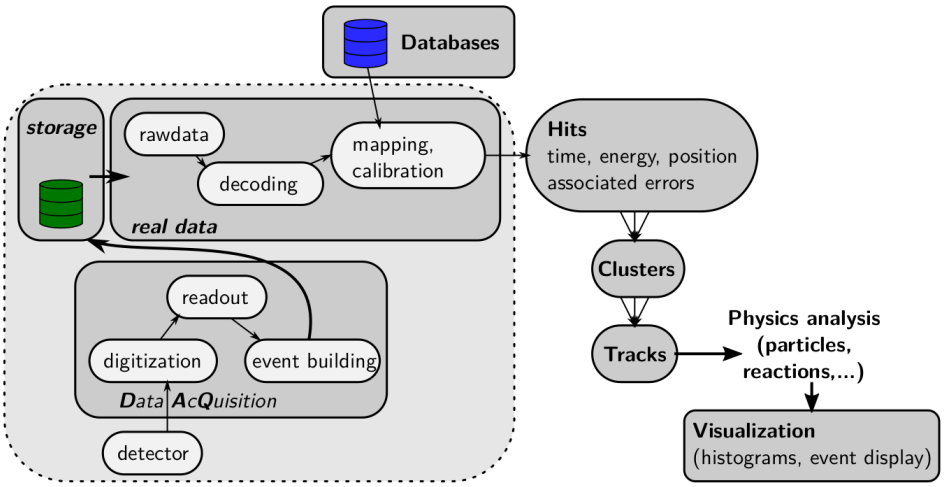

Figure 3.1: An illustration showing the various building blocks of the ExPLORA framework (from [37])

the errors and detector geometry are added to this data, and if the signal is above a certain energy threshold, it is stored as an object called a 'hit' in this framework. If multiple hits fulfill certain conditions such as being adjacent and correlated in time, they are grouped together as 'clusters' arising from the energy deposition of a single particle. When clusters for the same particle from a number of detectors are combined, the 'track' of this particle can be reconstructed. In the physics analysis, these tracks can be used as a basic input and combined with some selection criteria making it possible to reconstruct particles which in turn arise from the decay of a 'reaction candidate' [36].

In addition to analysis of the data collected in the BGOOD experiment, the ExPLORA framework is also used for generation of simulated data. This takes place in two main steps. First of all, the user specified reaction name, target type (hydrogen or deuterium) and reaction mechanism (coherent or incoherent production for a deuterium target) is taken as an input by the event generator, which then allocates masses and widths (as defined in the Particle Data Group booklet) to the initial and final state particles. The production threshold for the specified reaction is calculated and an initial state photon beam is generated, following a bremsstrahlung spectrum, with energies lying between the threshold and the electron beam energy. The final state particles are assigned momenta four vectors, either from a cross section (if it has already been measured for the reaction of interest) or sampled from phase space distributions (for which only the total initial state energy and masses of final state particles need to be known, and four momenta conservation has to be applied) [35]. In the second step, Monte Carlo methods are used to simulate decays of the final state particles, aided by information about the geometry of the detectors and the magnetic field in the BGOOD experiment. The Geant4 (**Ge**ometry **an**d **T**racking 4) toolkit is used for modelling the passage of these decaying particles and their energy losses [34].

3.1.2 Track reconstruction in different detectors

In this thesis, the central detector is used for identifying tracks of decay products arising from the $\Sigma(1385)$, which decays almost at rest and the forward spectrometer is used to identify the forward going K^+. The general scheme of particle identification in these detectors is therefore discussed in more detail in this section.

Tracks in the central calorimeter

The reconstruction of the central tracks is performed by information collected from the BGO ball and the scintillator barrel. The heavy charged particles, mostly undergo Bethe-Bloch ionization and deposit their energy in one or two neighbouring crystals. In contrast to this, the photons undergo bremsstrahlung and pair production, thereby producing electromagnetic showers and their energy deposition is spread out over a number of BGO crystals. Fig. 3.2 shows this difference in energy deposition between a proton and a photon in the BGO detector. In order to determine the position of a BGO cluster, a weighted average is taken over all the crystals [36]:

$$\bar{r} = \frac{\sum_i r_i \sqrt{E_i}}{\sqrt{E_i}} \tag{3.1}$$

To fully reconstruct the central tracks, the BGO clusters are associated with the hit information from the scintillator barrel, by looking at the azimuthal angle (ϕ) difference. A selection cut from $[-20, 20]°$. Further, a selection cut of $[-5, 5]$ ns is applied on the time difference between the event trigger and the time of the central tracks, to select the tracks to be used for further analysis [33].

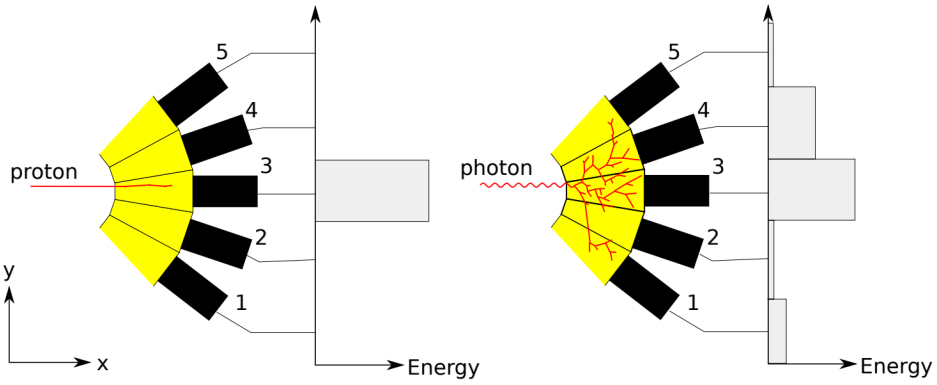

Figure 3.2: Illustration of the difference between tracks formed by a proton and a photon in the BGO calorimeter. The BGO crystals and PMTs are indicated by the yellow and black blocks respectively. The plots on the right of these figures show the energy deposition read out for each PMT channel (from [33])

Tracks in the forward spectrometer

The first part of the forward going tracks, upstream of the dipole magnet is reconstructed by using data from the MOMO and SciFi detectors. A mandatory requirement that a signal must be seen in both these detectors is enforced, in order to rule out any particles that do not arise from the target. Clusters in these two detectors are associated with clusters in the ToF walls, downstream of the magnetic field. This is done by first connecting the clusters in the MOMO and SciFi by a straight line and then extrapolating the track to the clusters in the ToF walls. This is done assuming that the track is a straight line in the vertical (xy) plane, as the magnetic field does not cause any deflection in this plane. This gives a rough estimate of the track in the forward spectrometer[34].This is further improved by including the closest hits in the drift chambers and also making fits to account for field non uniformities in fringe fields and Bethe-Bloch energy losses [36]. Depending on the particle type, momentum corrections are also applied, resulting in

the final tracks in the forward spectrometer.

Additionally, the relativistic velocity β is also determined from the track lengths and the timing information from the ToF walls. The masses of the forward going particles can then be easily calculated:

$$m = \sqrt{\left(\frac{p}{\beta}\right)^2 - p^2} \tag{3.2}$$

Plotting the reconstructed β vs. the reconstructed momenta results in 'banana-like' plots, each of the bands corresponding to a different particle, allowing for clean identification of particles in the forward spectrometer. These are shown in Fig. 3.3.

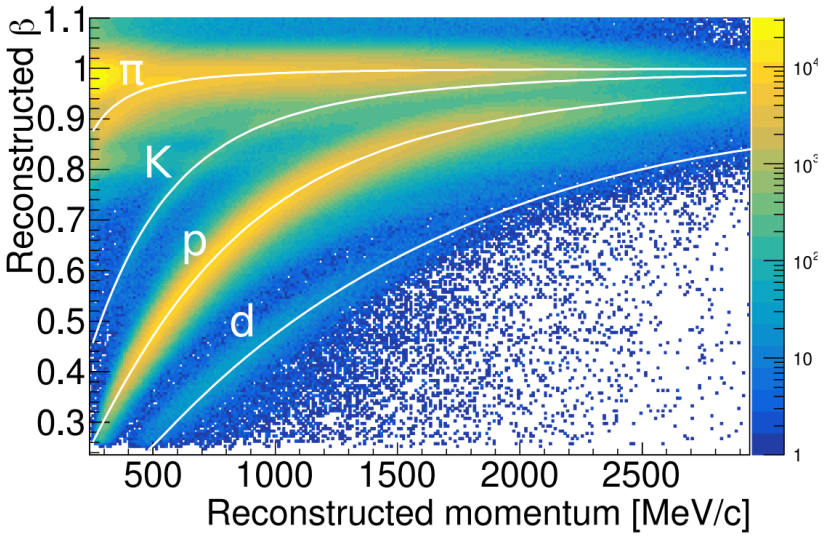

Figure 3.3: Plots of the reconstructed relativistic velocity (β) vs. the reconstructed momenta in the forward spectrometer. Each of the different forward going particles are indicated by the highlighted curves and corresponding labels (from [34])

3.2 Generation of simulated data

For the purpose of the analysis, two datasets were simulated using the ExPLORA event generator. The first one of these was the reaction of interest: $\gamma p \rightarrow K^+\Sigma(1385)$, and the second one was the dominant background for this reaction: $\gamma p \rightarrow K^+\Lambda(1405)$. A simulation of the latter is required as the $\Sigma(1385)$ and the $\Lambda(1405)$ are nearly mass degenerate and also have the same neutral decay final products (except for an additional photon carrying 76 MeV in the decay of the $\Lambda(1405)$; which is in fact crucial to distinguish these two final state particles). The $\Sigma(1385) \rightarrow \Lambda\pi^0$ is the dominant decay channel for the $\Sigma(1385)$ with a branching ratio of $\sim 87\%$. The $\Lambda(1405) \rightarrow \Sigma\pi^0$ branching ratio is 100%. The neutral decay schemes of both these baryons are shown in Fig. 3.4.

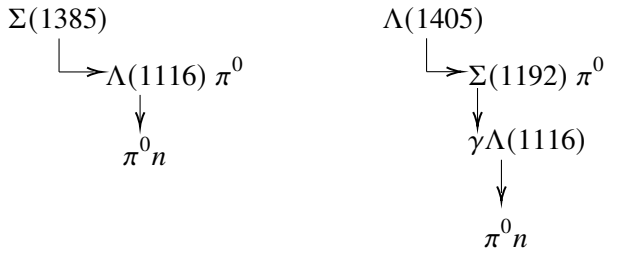

(a) Decay of $\Sigma(1385) \rightarrow \Lambda\pi^0$ (b) Decay of $\Lambda(1405) \rightarrow \Sigma\pi^0$

Figure 3.4: Neutral decay schemes of the $\Sigma(1385)$ and $\Lambda(1405)$

3.3 Event Selection

In order to filter out the events of interest for the analysis, a number of preliminary cuts are initially applied to the large experimental dataset as well as to the simulated data. This includes at least two neutral tracks in the BGO calorimeter (corresponding to the detection of a minimum of two photons, arising from a π^0 decay) and a photon beam energy in the range of 900 – 3000 MeV (the lower limit is set around the strangeness threshold, i.e. the minimum amount of energy required to produce a K^+K^- pair). Further conditions are applied to select events in which a K^+ is observed: at least one track in the forward spectrometer, a minimum of one charged track in all the detectors and charge of particles in the forward spectrometer must be +1.

	Cuts	**Description**
Preliminary	$n^0_{\mathrm{BGO}} \in [2, 300]$	no. of neutral tracks in the BGO
	$n_{\mathrm{FS}} \in [1, 300]$	no. of tracks in the forward spectrometer
	$n^{\mathrm{ch}}_{\mathrm{tot}} \in [1, 300]$	total no. of charged tracks
	$q = +1$	charge of particle in the forward spectrometer
	$E_\gamma \in [900, 3000]$ MeV	beam energy
Selection	$n^0_{\mathrm{BGO}} = 4$	no. of photons in the BGO
	$n_{\mathrm{FS}} = 1$	no. of tracks in the forward spectrometer
	$n_{\mathrm{SiRi}} = 0$	no. of tracks in the SiRi
	$n^{\mathrm{ch}}_{\mathrm{BGO}} = 0$	no. of charged tracks in the BGO
	$\cos\theta^{\mathrm{K}^+}_{\mathrm{CM}} \in [0.9, 1.0]$	cosine of the polar angle of the K^+ in the CM frame
	$m_{\mathrm{K}^+} \in [444, 544]$	cut on measured mass in the forward spectrometer
	$m_{\pi^0} \in [105, 165]$	cut on measured mass of 2γ combination in the BGO

Table 3.1: A table summarizing the cuts applied on the datasets for the analysis

After application of these cuts, data files of a much more manageable size are obtained, which can then be analyzed using a local installation of the ROOT framework. Now, more stringent cuts are used : the number of charged tracks in the BGO and the tracks in SiRi (the intermediate detector) are required to be zero, since these tracks do not occur in the event topology of this photoproduction reaction. Further, the number of tracks in the forward spectrometer is set to one, so that events with only one forward

going meson are selected, and the number of neutral tracks in the BGO is required to be four, since two π^0's (which subsequently decay to four photons) arise in the decay schemes of both the $\Sigma(1385)$ and $\Lambda(1405)$. Also, an angular cut from 0.9 to 1.0 is applied on cosine of polar angle of the outgoing meson, meaning that only events in the very forward region (25.8° to 0°) are selected.

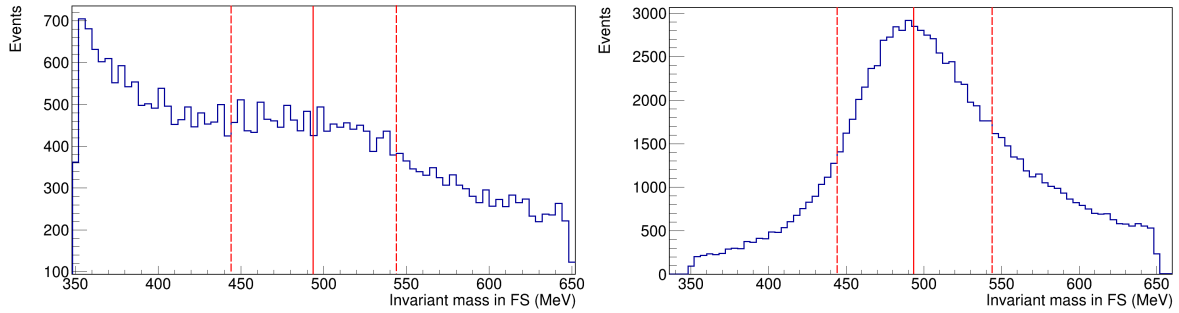

(a) Experimental data

(b) Simulated data for $\gamma p \rightarrow K^+\Sigma(1385)$

Figure 3.5: Histograms of the reconstructed mass in the forward spectrometer. The solid and dashed red lines indicate the K^+ nominal mass and the $\pm 2\sigma$ mass selection cuts respectively. In the experimental data, the K^+ peak is smeared out with a significant background from the π^+ mass distribution which can be seen on the lower end. This background is absent in the simulated data, as expected.

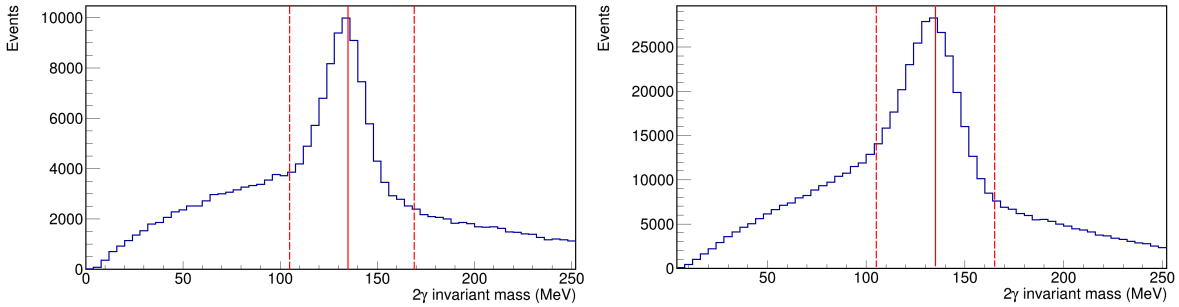

(a) Experimental data

(b) Simulated data for $\gamma p \rightarrow K^+\Sigma(1385)$

Figure 3.6: Histograms of the 2γ invariant mass in the central calorimeter. The vertical solid and dashed lines again indicate the π^0 nominal mass, $\pm 2\sigma$ mass selection cuts respectively.

Finally, in order to select only the positively charged kaons in the forward spectrometer, a mass cut of ±50 MeV is placed, centered around ($\pm 2\sigma$) the nominal K^+ mass. It is to be noted that before imposing this selection cut, the reconstructed mass in the forward spectrometer is corrected by a small momentum dependent factor (explained in Sec. 3.3.1). For the measured two photon invariant mass in the BGO calorimeter, only two photon combinations that have an invariant mass of ±30 MeV (i.e. $\pm 2\sigma$) around the actual π^0 mass are identified as neutral pions. All the preliminary and selection cuts are shown in Table 3.1. The selection cuts for the K^+ on the reconstructed mass in the forward spectrometer are displayed in Fig. 3.5. In Fig. 3.6, selection cuts are similarly shown for the π^0 identification in the central calorimeter.

3.3.1 Forward spectrometer mass and momentum corrections

As a result of the detector geometry and magnetic field not being accounted for perfectly, it is seen in the experimental data (and to a lesser extent in the simulated data) that there is a slight shift in the reconstructed mass of forward going particles with their momenta. To account for this shift, the K^+ mass is first corrected by a fraction of the nominal proton mass [38]:

$$m'_{K^+} = m_c \cdot m_{K^+} = \left(\frac{m_p}{m_{p'}}\right) m_{K^+} \tag{3.3}$$

where m'_{K^+} is the corrected K^+ mass, m_c the correction factor, m_{K^+} the uncorrected K^+ mass, m_p the nominal proton mass and m'_p the corrected proton mass. m_c is the ratio of the uncorrected and corrected proton mass. $m_{p'}$ is a function of the measured momentum magnitude ($|\vec{p}|$) and the angles that the trajectory of the forward going particle makes with the beam axis (θ_x, θ_y):

$$m_{p'} = m_{p'}(|\vec{p}|, \theta_x, \theta_y) \tag{3.4}$$

with θ_x and θ_y defined as:

$$\theta_x = \tan^{-1}\left(\frac{p_x}{p_z}\right) \tag{3.5}$$

$$\theta_y = \tan^{-1}\left(\frac{p_y}{p_z}\right) \tag{3.6}$$

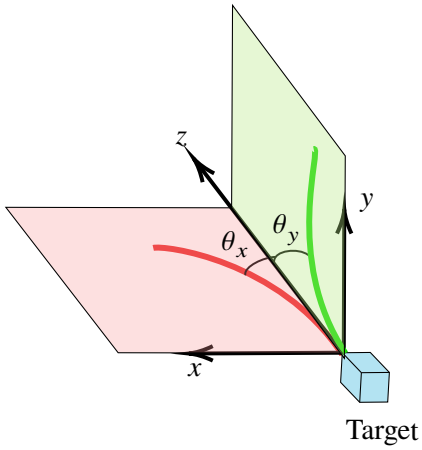

Figure 3.7: An illustration showing the angles θ_x and θ_y, as seen from the target in the direction of the outgoing beam. The z axis is the beam axis and the red and green solid lines are projections of the trajectory of the forward going particles.

For the purpose of performing the corrections, the angles θ_x and θ_y are discretized in integer steps. For each combination of θ_x and θ_y, a quadratic fit is made to the plot of the reconstructed proton mass vs. its momentum. All of these fits are stored in a separate correction file. The explicit form of the corrected

proton mass, $m_{p'}$ is:

$$m_{p'} = f_{X,Y}(1-\Delta X)(1-\Delta Y) + f_{X',Y}\Delta X(1-\Delta Y) + f_{X,Y'}(1-\Delta X)\Delta Y + f_{X',Y'}\Delta X\Delta Y \tag{3.7}$$

Here, $f_{X,Y}$ is the (previously mentioned) quadratic fit function for the discretized values of θ_x and θ_y, evaluated at a particular momentum ($|\vec{p}|$). $f_{X',Y}$ is likewise the evaluated fit function for the nearest neighbouring discretized value of θ_x ($X+1$) and the same value of θ_y (Y) and so on. ΔX and ΔY are defined as the deviations of the actual θ_x and θ_y from the corresponding discretized values X and Y:

$$\Delta X = \theta_x - X \tag{3.8}$$

$$\Delta Y = \theta_y - Y \tag{3.9}$$

The corrected proton mass (for a particular combination of θ_x, θ_y and $|\vec{p}|$) can then be understood to be an average of the values of the proton mass determined from the fits over nearest integer values of θ_x and θ_y, weighted by the deviation of the actual angles from their discretized values. As an example a plot of the dependence of the reconstructed proton mass on its magnitude of momentum, along with a quadratic fit to the data is shown in Fig. 3.8.

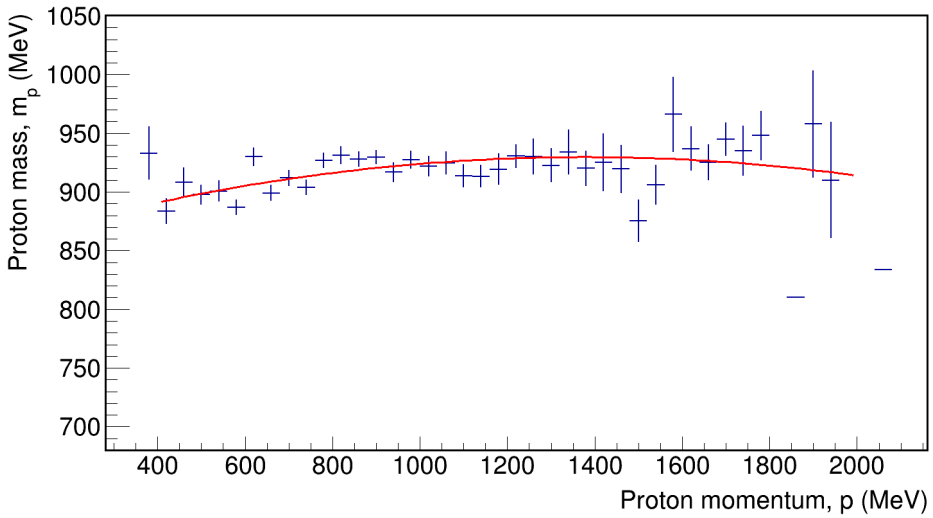

Figure 3.8: A plot of the reconstructed proton mass vs. the magnitude of its momentum for particular values of the discretized θ_x and θ_y (here $(X,Y) = (-10°, 2°)$). The red solid line is a second order polynomial fit to the data.

Subsequent to K^+ mass correction, K^+ selection cuts are applied to this corrected kaon mass, as described in the previous section. Thereafter the K^+ momentum is corrected ($|\vec{p}'_{K^+}|$) and the kaon energy is recalculated (E'_{K^+}) in such a way that the measured kaon mass gets fixed to its nominal value (493.67 MeV):

$$|\vec{p}'_{K^+}| = m_c \cdot |\vec{p}_{K^+}| \tag{3.10}$$

$$E'_{K^+} = \sqrt{493.67^2 + |\vec{p}'_{K^+}|^2} \tag{3.11}$$

3.3.2 Selection of background data

Since the light π^+'s are seen in large numbers in the forward spectrometer, it is likely that the higher end of the measured π^+ mass distribution might have an overlap with the mass selection cut for the K^+ and some π^+ events may thereby get misidentified as K^+'s. To account for this, a 'background' dataset is extracted from the experimental data by applying a lower sideband cut from 300 to 400 MeV (instead of the previously mentioned $[444, 544]$ MeV for a K^+) on the measured mass in the forward spectrometer. This background is later used while making fits to the experimental data and extracting the yield, which is discussed in Section 3.4.

3.3.3 Double counting of photons

It is seen that among all possible two photon combinations that are identified as π^0's, there can be cases of double counting of photons. For example, a photon arising from the decay of the first π^0 may be counted again along with a photon coming from the second π^0, giving a falsely reconstructed π^0. Therefore, identifying two photon combinations as pions simply based on the requirement that their combined invariant mass falls in the mass selection window for a π^0 is not enough to rule out these falsely identified pions. Therefore, an additional condition is applied after the pion mass selection cut: if either of the photons from the first π^0 has the same four momentum as that of a photon from the second π^0, then these two π^0 combinations are rejected. Fig. 3.9 shows the measured mass in the BGO calorimeter before and after the elimination of unphysical $2\pi^0$ combinations.

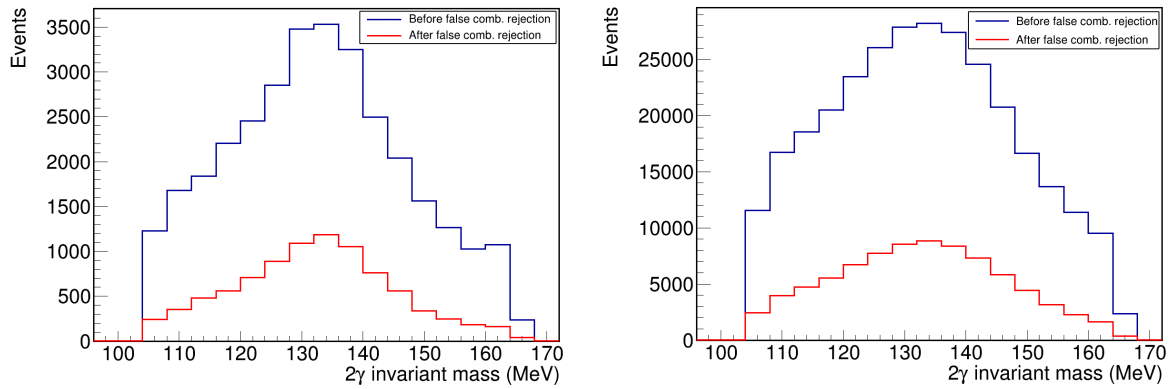

(a) Experimental data

(b) Simulated data for $\gamma p \rightarrow K^+\Sigma(1385)$

Figure 3.9: Histograms of the π^0 mass distribution in the BGO calorimeter, before (blue) and after (red) rejecting the unphysical two π^0 combinations.

Following the selection of only the physical 2γ combinations, their masses are fixed to the nominal pion mass, m_{π^0} (134.98 MeV).

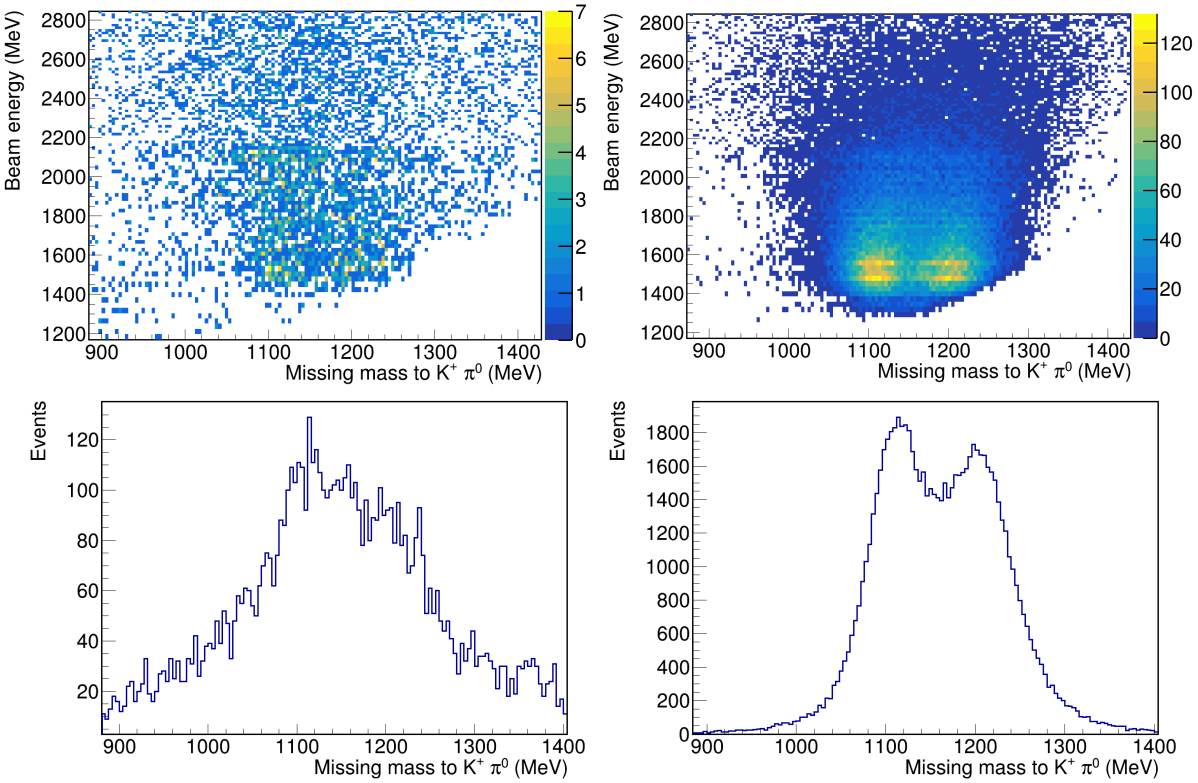

(a) Experimental data

(b) Simulated data for $\gamma p \rightarrow K^+\Sigma(1385)$

Figure 3.10: 2D distributions of the beam energy v/s the missing mass to $K^+\pi^0$ and their projections (integrated over all beam energies)

3.4 Yield extraction

3.4.1 Missing mass distributions

For extracting the yield, i.e. the number of $K^+\Sigma(1385)$ events, one needs to separate out the $K^+\Lambda(1405)$ final state and also background events (arising from π^+ being misidentified as K^+) from the experimental data. To do so, it is not sufficient to look at the missing mass to K^+, as the $\Sigma(1385)$ and $\Lambda(1405)$ are almost mass degenerate (as discussed in Section 3.2). Therefore distributions of the missing mass to $K^+\pi^0$ and $K^+\pi^0\pi^0$ are studied.

Firstly, the two dimensional distributions of the beam energy v/s the missing mass to $K^+\pi^0$ are plotted out for all the datasets: the experimental data, $\gamma p \rightarrow K^+\Sigma(1385)$ and $\gamma p \rightarrow K^+\Lambda(1405)$ simulated data and also the background data. Subsequently their projections onto the x axis (i.e. the missing mass axis) are taken. As an example, these distributions for the experimental data and the $\gamma p \rightarrow K^+\Sigma(1385)$ simulated dataset is shown in Fig. 3.10. In the simulated dataset for $\gamma p \rightarrow K^+\Sigma(1385)$ the first peak around 1116 MeV is from ground state Λ baryon, which can be seen to arise when taking the missing mass to the K^+ and the first π^0 in the $\Sigma(1385)$ decay scheme (Fig. 3.4). The second peak around 1200 MeV is from a neutron and a π^0 which is the second possibility when one considers the missing mass to the K^+ and the other π^0 in the decay scheme. It is to be noted that although the added rest masses

of the neutron and π^0 amounts to around 1075 MeV; this two body system can carry a certain amount of kinetic energy, which is why the peak corresponding to this system is seen at a higher energy.

In the corresponding missing mass distribution for $\gamma p \rightarrow K^+\Lambda(1405)$, a peak around 1200 MeV is seen, which contains the peak arising from the ground state Σ baryon in addition to the $\gamma\pi^0 n$ distribution (which arises when one considers the second possibility for missing mass to $K^+\pi^0$, see Fig. 3.4). The experimental dataset contains an overlap of all these contributions, and the background data more or less replicates the shape of the experimental data. These distributions for the $\gamma p \rightarrow K^+\Lambda(1405)$ simulated data and background are shown in the Appendix A.1.

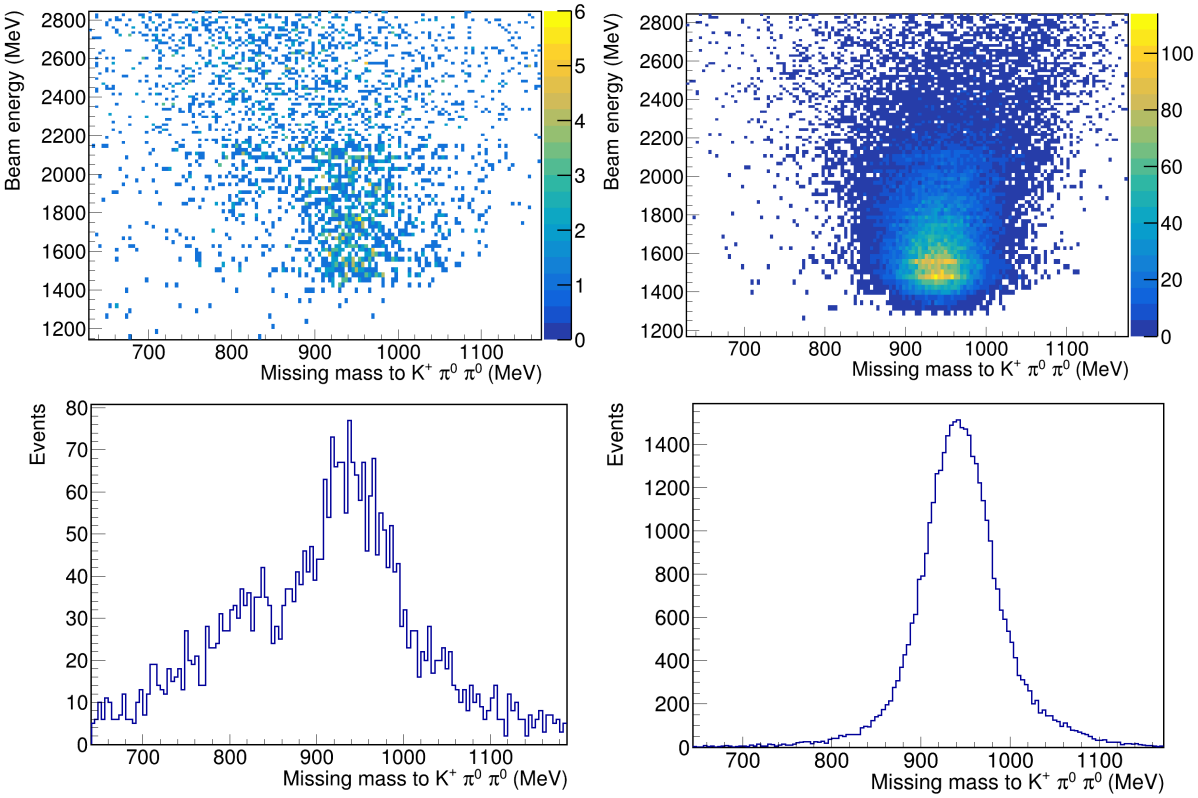

(a) Experimental data

(b) Simulated data for $\gamma p \rightarrow K^+\Sigma(1385)$

Figure 3.11: 2D distributions of the beam energy v/s the missing mass to $K^+\pi^0\pi^0$ and their projections (integrated over all beam energies)

Similarly, the missing mass to $K^+\pi^0\pi^0$ distributions for all the aforementioned datasets were also plotted. Fig. 3.11 shows these for the experimental data and the $\gamma p \rightarrow K^+\Sigma(1385)$ simulated data. In the distribution for $\gamma p \rightarrow K^+\Sigma(1385)$ simulated data, there's a single peak around 939 MeV arising from a neutron in the decay scheme. In the distribution for simulated $\gamma p \rightarrow K^+\Lambda(1405)$ data, the peak is centered at 1018 MeV. From the $\Lambda(1405)$ decay scheme, one sees that this is close to the added energy of the decay photon (carrying 76 MeV) and the rest mass of the neutron and thus is the γn distribution. These missing mass distributions for simulated $\gamma p \rightarrow K^+\Lambda(1405)$ datasets and the background are again shown in Appendix A.1.

3.4.2 Fitting simulated datasets to the experimental data

In order to get an energy dependent yield, projections of the (two dimensional) missing mass distributions onto the beam energy axis are taken. Subsequently, these projections are binned out in a number of energy bins. The energy ranges of these projections are taken to be the same as the tagger bin widths.

Each of the projections for the experimental data is now fitted with projections for the two simulated channels ($\gamma p \rightarrow K^+\Sigma(1385)$, $\gamma p \rightarrow K^+\Lambda(1405)$) and the background data. This is done both for the distributions for missing mass to the $K^+\pi^0$ as well as to the $K^+\pi^0\pi^0$ systems. An example of these fits for beam energy range E_γ = 1544.23 − 1570.99 MeV is shown in the Fig. 3.12.

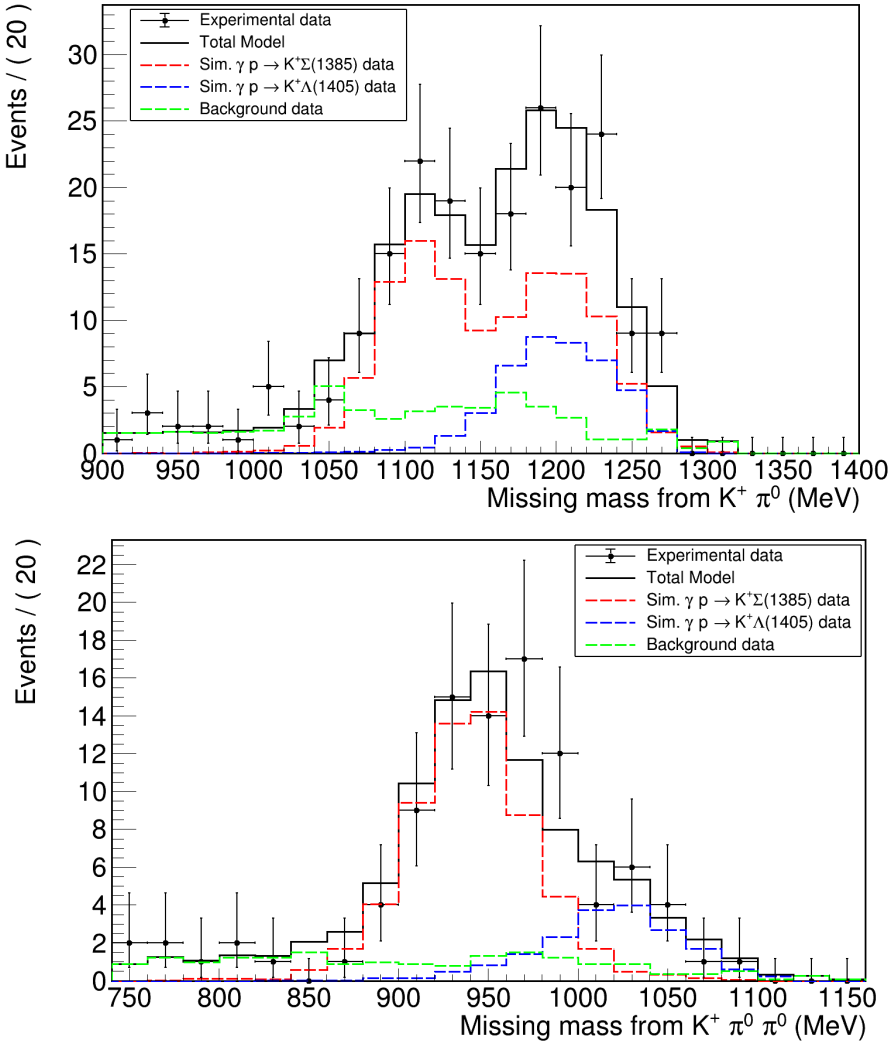

Figure 3.12: Fits to the experimental data using simulated and background data for the missing mass distributions (E_γ = 1544.23 to 1570.99 MeV). The black solid line is the model constructed by adding together the contributions from the $\gamma p \rightarrow K^+\Sigma(1385)$ (red dashed line), $\gamma p \rightarrow K^+\Lambda(1405)$ (blue dashed line) and the background (green dashed line) data. The top figure shows the fits for the missing mass from $K^+\pi^0$ distribution and the bottom one shows it for the missing mass from $K^+\pi^0\pi^0$ distribution

In order to estimate the yield, the RooFit toolkit is used which performs binned maximum likelihood fits. Each of the datasets are modelled as probability density functions and a composite model is created, where these individual pdfs are added together. The following input parameters are provided: the range over which the fit is to be performed, initial values for the fraction of events in the experimental data that can be attributed to each dataset and the minimum and maximum bounds within which these values are allowed to vary. RooFit uses built in minimization algorithms such as the MINUIT algorithm to minimize the negative log likelihood function [39]. When a sufficiently good fit is attained, the yield, or the number of events (in the experimental data) coming from $\gamma p \rightarrow K^+\Sigma(1385)$ is obtained. Since this procedure is done for each energy bin, the energy dependence of the yield can be plotted and is shown for the missing mass to the $K^+\pi^0$ and missing mass to the $K^+\pi^0\pi^0$ distributions in Fig. 3.13. It is observed that the yield for the missing mass to $K^+\pi^0$ is nearly twice as high as that from the other distribution. This is because of the fact that this histogram is filled two times, once for each of the two possible combinations of a K^+ and a π^0.

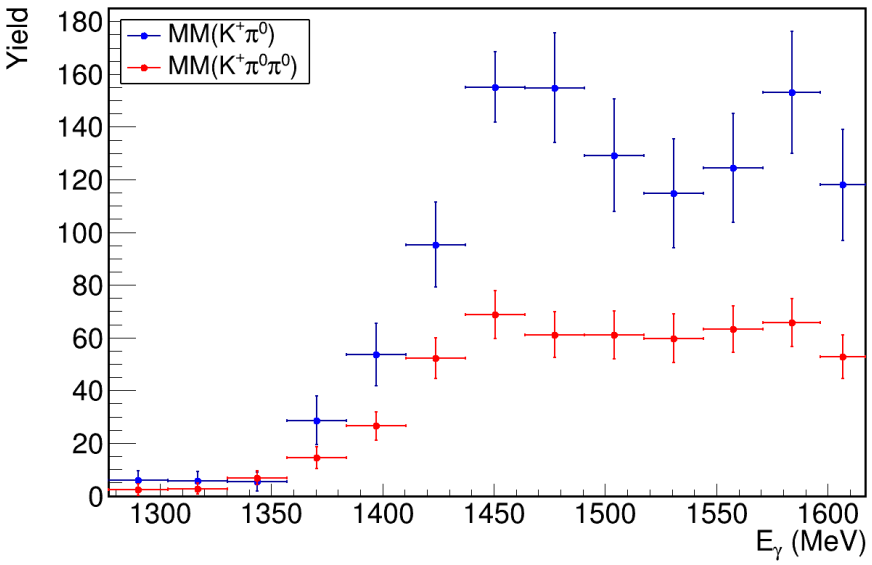

Figure 3.13: Raw yields for the two missing mass distributions, namely the missing mass to $K^+\pi^0$ (in blue) and missing mass to $K^+\pi^0\pi^0$ (in red)

3.4.3 Normalization with photon flux

The raw yield of the $K^+\Sigma(1385)$ final state events is by itself not very useful, as one also needs to account for the fact that the flux of photons varies with the beam energy and that the energy bins do not have the same size. Therefore, it is necessary to normalize this raw yield by the photon flux distribution [40]. The photon flux histogram and the normalized yields for the $K^+\Sigma(1385)$ events (using the two missing mass techniques) are shown in Fig. 3.14 (a) and (b) respectively.

The flux distribution is found to follow the expected $1/E_\gamma$ distribution. The steps and the variable energy bin sizes arise due to the fact that the tagger hodoscope is constructed out of plastic scintillators having five different energy resolutions ranging from $0.4\%E_0$ for the horizontal scintillators to $0.6 - 1.7\%E_0$ for the vertical ones [32] (E_0 being the initial beam energy).

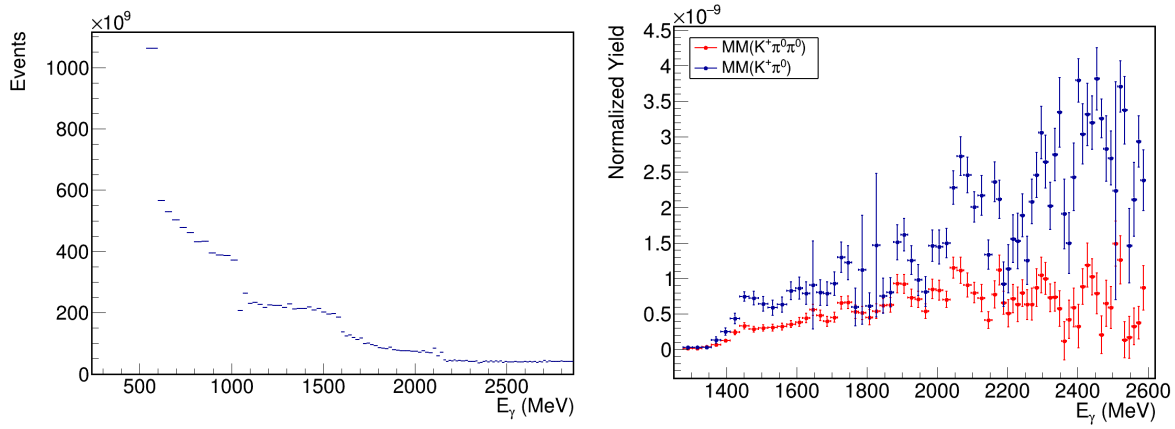

(a) (b)

Figure 3.14: Histograms of the (a) photon flux distribution and (b) normalized yields for $K^+\Sigma(1385)$ final state events

3.5 Target area density and solid angle

The next ingredient used in the differential cross section is the area density of the liquid hydrogen target:

$$\rho_A = n \cdot l \tag{3.12}$$

where n is the density of the liquid hydrogen target (at 18 K) and l is the effective length of the target cell (taken as 6.1 cm for the short target). The density of the Mylar foil surrounding the target is also accounted for. This gives a target area density of 2.58×10^{-7} μb^{-1} (from Georg Scheluchin's PhD thesis [33]).

It is also necessary to find the solid angle $d\Omega$ over which the final state particles are scattered in this reaction:

$$d\Omega = \int_{\phi_1}^{\phi_2} \int_{\theta_1}^{\theta_2} \sin\theta d\theta d\phi \tag{3.13}$$

One sees that since an unpolarized beam and target are used in this study, the angular distribution would be azimuthally (in ϕ) isotropic, meaning that we can integrate over the entire range of ϕ, i.e. $\phi = 0$ to 2π. Also, we are investigating the reaction only at very forward (polar) angles (of the outgoing K^+ in the center of mass frame), so we integrate from $\cos\theta^{K^+}_{\mathrm{CM}} = 0.9$ to 1. This gives a factor of:

$$d\Omega = \int_{\phi_1=0}^{\phi_2=2\pi} d\phi \int_{\cos\theta_1=0.9}^{\cos\theta_2=1} d(\cos\theta) = 0.2\pi \tag{3.14}$$

3.6 Reconstruction efficiency

It is expected that the number of events that are measured by the detectors and pass all the selection cuts of the analysis are only a fraction of the total number of events that occur in this reaction; this ratio is called the reconstruction efficiency. However, as there is no way to accurately establish the total events in the experimental data, the dataset for the ($K^+\Sigma(1385)$ final state) generated by Monte Carlo simulations

is used. The reconstruction efficiency is then calculated by taking the ratio of the identified events to the total generated events:

$$\epsilon(E_\gamma, \theta) = \frac{N_{\text{sim}}^{\text{identified}}}{N_{\text{sim}}^{\text{generated}}} \tag{3.15}$$

Various known factors that play a role in the overall efficiency, such as the branching ratios of the final state particles (such as for $\pi^0 \rightarrow \gamma\gamma$) and detector efficiencies are modeled into the simulation.

The determined efficiencies for the two missing mass channels are shown in Fig. 3.15. The peak efficiency for the missing mass to $K^+\pi^0$ distribution is found to be at 2.85% and for the the missing mass to $K^+\pi^0\pi^0$ distribution is at 1.43%. As expected the two efficiencies have a relative factor of two, following the same behaviour as for the yields in Section 3.4. This factor of two however has ultimately little to no effect on the differential cross section estimation using the two methods as it cancels out (the yield is the numerator and efficiency in the denominator in the final expression) as would be evident in Section 3.7.

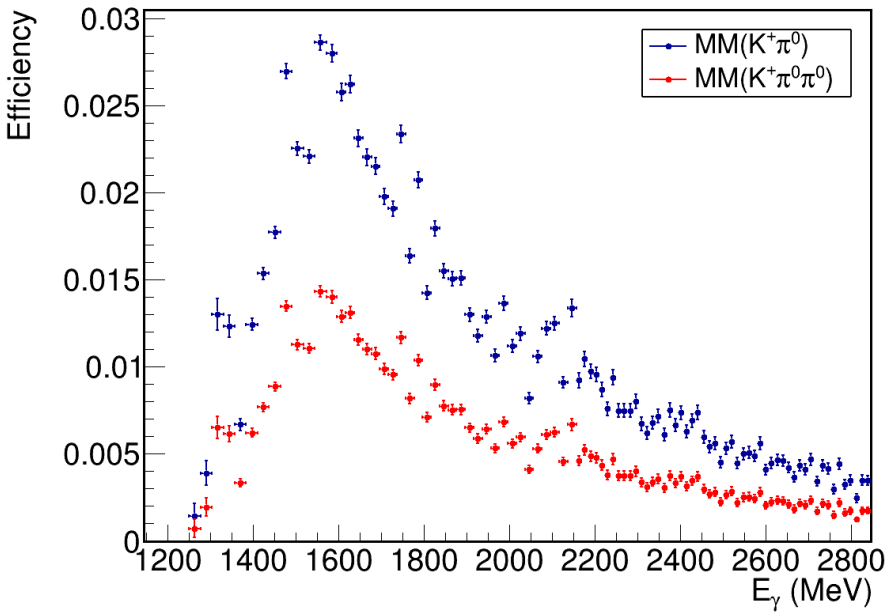

Figure 3.15: Reconstruction efficiency for the missing mass to $K^+\pi^0$ (in blue) and $K^+\pi^0\pi^0$ distributions (in red)

3.7 Putting it all together: differential cross section

The differential cross section for the photoproduction process under study is given by the equation:

$$\frac{d\sigma}{d\Omega}(E_\gamma, \theta) = \frac{Y(E_\gamma, \theta)}{F(E_\gamma)} \cdot \frac{1}{\rho_A \cdot \epsilon(E_\gamma, \theta) \cdot d\Omega} \tag{3.16}$$

Here, the first term gives the normalized yield of the $K^+\Sigma(1385)$ final state, i.e. the raw yield scaled down by the photon flux as described before in Section 3.4. In the second term, ρ_A is the target area

density which was found to be 2.58×10^{-7} μb^{-1} in Section 3.5 and $d\Omega$ being the solid angle (amounting to a factor of 0.2π). All the aforementioned calculated factors and measured quantities are put together to arrive at the differential cross section for the photoproduction process: $\gamma p \rightarrow K^+\Sigma(1385)$ with the outgoing K^+ at forward angles ($\cos\theta^{K^+}_{CM} = 0.9$ to 1). Although the differential cross section can be shown in terms of the photon energy in the laboratory frame, it is often convenient to work in the center of mass frame. As such the differential cross section with respect to the center of mass energy (W), for the process under investigation is shown in Fig. 3.16. As can be seen, the resulting differential cross

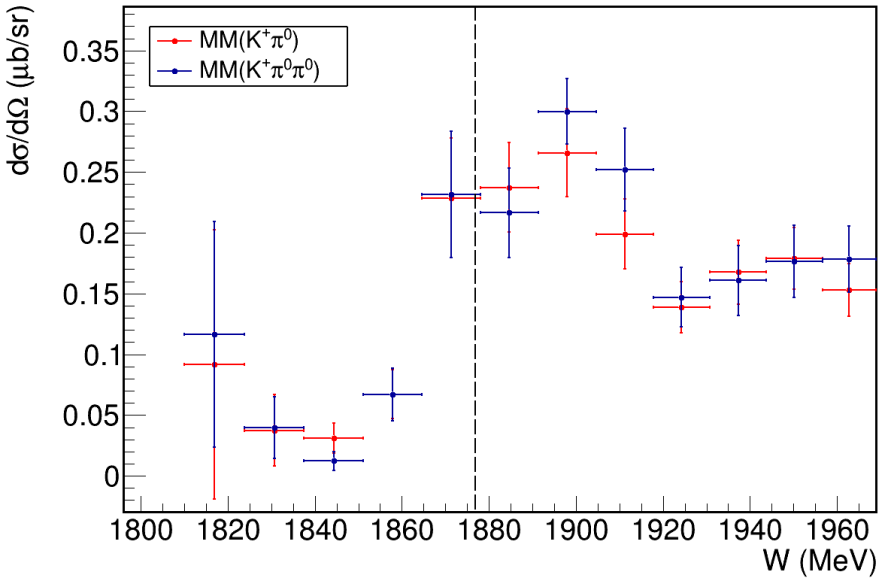

Figure 3.16: The differential cross section for the process $\gamma p \rightarrow K^+\Sigma(1385)$ ($\cos\theta^{K^+}_{CM} = 0.9$ to 1) using the missing mass to $K^+\pi^0$ (in blue) and $K^+\pi^0\pi^0$ (in red) distributions. The production threshold for the $K^+\Sigma(1385)$ is indicated by the black dashed line. It is to be noted that the threshold value indicated here is in fact using the nominal mass of the $\Sigma(1385)$. Since the $\Sigma(1385)$ has finite width (±36 MeV), the production threshold is smeared around the indicated value.

sections from the two missing mass reconstruction techniques are in very good agreement (within 1σ) of each other. It is to be noted that the two missing mass distributions arise from the same measured dataset and are therefore correlated, which could be leading to such a good agreement between the differential cross sections from the two techniques. Differential cross section values beyond center of mass energies of 1970 MeV are not shown here, as at higher energies the reconstruction of the final states is itself not very reliable. It is complicated by the fact that there might also be additional backgrounds such as those from the K^* final states which have not been accounted for. However for the purpose of studying this photoproduction process in the context of a possible bound hadronic state of the K^+ and $\Sigma(1385)$, it is sufficient to accurately determine the differential cross section around the production threshold ($\sim$ 1876 MeV) which has been done here. A physical interpretation of this differential cross section is discussed in the next chapter.

3.8 Evaluation of systematic uncertainties

Table 3.2 shows the individual and overall systematic uncertainties on the differential cross section of $\gamma p \rightarrow K^+\Sigma(1385)$. The overall systematic uncertainty is found by summing all the individual systematic uncertainties in quadrature and then taking the square root, arriving at a value of 11.5%. Some of the sources of the uncertainties are independent of the process under study, such as those related to the beam position (where it hits the target), determination of photon flux, target length, efficiencies of various detectors and different triggers. These are therefore taken to be the same as determined in a paper on $K^+\Lambda$ photoproduction ([41]) at the same experimental setup. Furthermore, as similar analysis steps have been adopted in Ref. [41], the uncertainty on the K^+ selection is kept as it is. For the π^0 selection, since two π^0's are selected here, compared to one π^0 in Ref. [41], therefore the uncertainty on π^0 selection is taken twice as much at 2%. An additional source of uncertainty depends on the fitting techniques used

Source	**Error (in %)**
Beam spot alignment	4.0
Photon flux	4.0
SciFi efficiency	3.0
K^+ selection	2.0
π^0 selection	2.0
Target wall contribution	2.0
Track time selection	2.0
Target length	1.7
ToF wall efficiency	1.5
MoMo efficiency	1.0
Drift chamber efficiency	1.0
Beam energy calibration	1.0
Forward track geometric selection	1.0
Modelling of hardware triggers	1.0
Fitting uncertainity	8.1
Total systematic uncertainty	**11.5**

Table 3.2: Systematic uncertainties for the estimation of the differential photoproduction cross section of $\gamma p \rightarrow K^+\Sigma(1385)$

to determine the yield and thereby the cross section. In order to determine this, firstly the ratio (R) of the differential cross sections determined using the two techniques is taken:

$$R = \frac{(d\sigma/d\Omega)_{\mathrm{MM}(K^+\pi^0\pi^0)}}{(d\sigma/d\Omega)_{\mathrm{MM}(K^+\pi^0)}} \tag{3.17}$$

The plot of this ratio v/s the center of mass energy (W) is then fitted with a constant line of the form:

$$R = c \tag{3.18}$$

This is shown in Fig. 3.17 alongwith the determined value of the constant and the reduced χ^2 value as a measure of goodness of the fit. It is seen that the ratio of the differential cross sections around $W = 1844$ MeV has a larger value of around 2.53. This is caused by the fact that the value of the measured differential cross sections (for the two missing mass techniques) is quite small (almost close to 0) for this energy bin, as such the ratio becomes much larger than for the other data points. This data point is however, still in agreement with the fitted line, within the corresponding error bars.

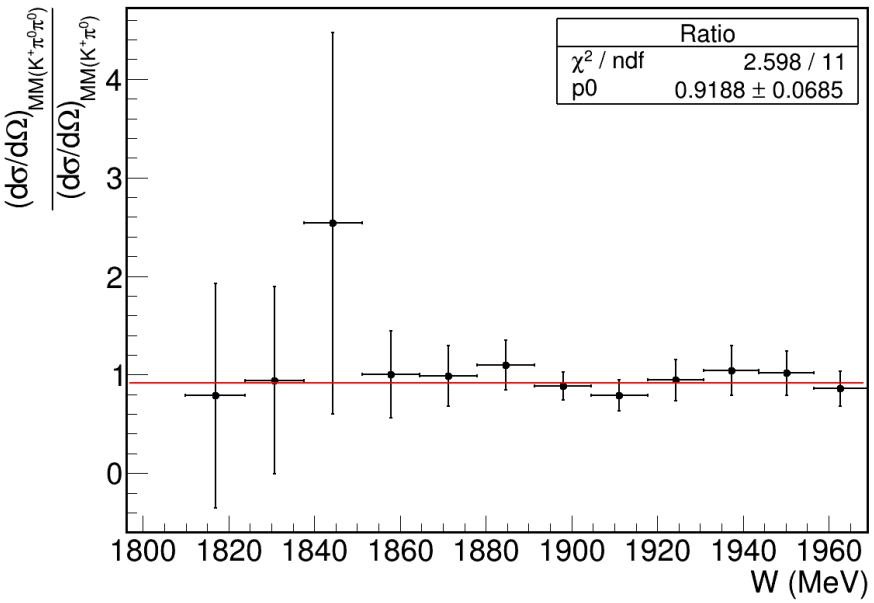

Figure 3.17: The ratio of the differential cross sections of $\gamma p \rightarrow K^+\Sigma(1385)$ determined using missing mass to $K^+\pi^0\pi^0$ and missing mass to $K^+\pi^0$, plotted v/s the center of mass energy (W). The constant line fit is shown in red. The reduced χ^2 value and the fitted constant (here $p0$) are also shown.

The difference of the fitted constant from 1 (i.e. the ideal ratio of the differential cross sections) then gives an approximate upper estimate of the fitting error at around 8.1%:

$$\sigma_{\text{fitting}} = 1 - c \approx 1 - 0.919 = 0.081 \tag{3.19}$$

CHAPTER 4

Results and Discussion

4.1 Physical interpretation of the differential cross section for $\gamma p \rightarrow K^{+}\Sigma(1385)$

The measured differential cross section (using the two missing mass techniques) is once again shown in Fig. 4.1, alongwith the overall systematic uncertainty and a pure pion exchange 'toy model' (discussed in Section 4.2).

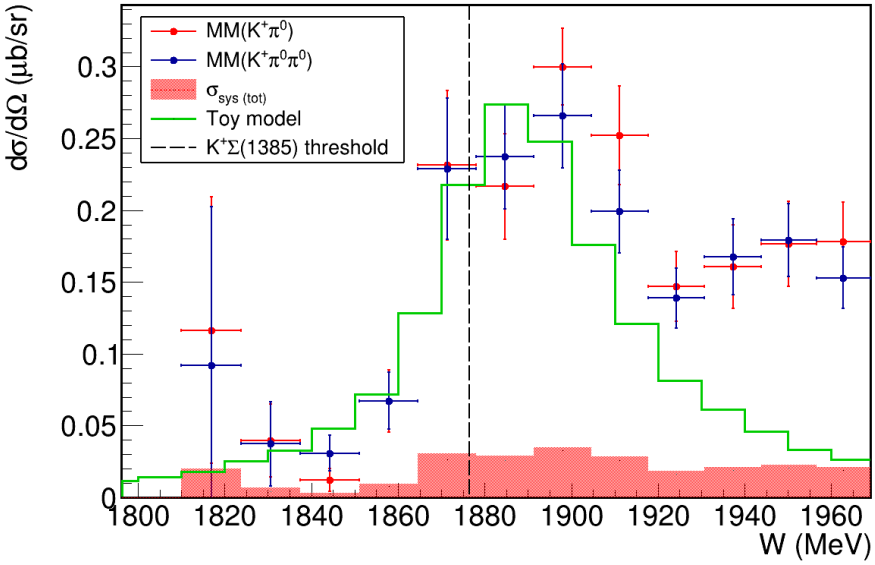

Figure 4.1: The measured differential cross section of $\gamma p \rightarrow K^{+}\Sigma(1385)$ v/s the center of mass energy (W), overlaid with the 'toy model'. The total systematic uncertainty is also indicated (red shaded region) along with the nominal $K^{+}\Sigma(1385)$ production threshold (black dashed line).

One finds that there is a three fold increase in the differential cross section from 0.07 $\mu b/\text{sr}$ at 1858 MeV to about 0.23 $\mu b/\text{sr}$ around 1871 MeV. Subsequently, the differential cross section attains a peak value of around 0.3 $\mu b/\text{sr}$ at a center of mass energy of $W = 1898$ MeV. Interestingly, this

peaking behaviour of the differential cross section is just around the $K^+\Sigma(1385)$ production threshold of 1876 MeV, which is also quite close to the predicted mass of a $K\Sigma^*$ bound state at 1872.6 MeV with $J^P = (3/2)^-$ (*Huang. et. al*, [31]).

As this process is occurring at very forward angles and just near the threshold, here the momentum difference (between the incoming photon and the outgoing K^+) squared, denoted by the Mandelstam variable t is minimal, i.e:

$$t = (p_\gamma - p_{K^+})^2 \rightarrow 0 \tag{4.1}$$

This in turn implies that the momentum transferred to the $\Sigma(1385)$ is minimal in this region. One can also understand this in the rest frame of the K^+: the momentum carried by the $\Sigma(1385)$ (relative to the K^+) in this frame is again minimum at the threshold. This condition makes it likely for a bound molecular state of the K^+ and $\Sigma(1385)$ to exist. The presence of the bound state is reflected in a resonance like structure in the differential cross section of $\gamma p \rightarrow K^+\Sigma(1385)$ as seen in Fig. 4.1. As long as the momentum transfer remains minimal or is comparable to the binding energy of this hadronic molecule, the system can stay bound together. At center of mass energies much beyond the threshold, the momentum transfer is sufficient to break apart the bound system, resulting in the production of K^+ and $\Sigma(1385)$ as separate, free entities. This can be seen in the slowly increasing value of the differential cross section beyond 1920 MeV (which is also accompanied by other background processes which might not have been accounted for).

Further, as the peak is just at the value of $W \approx 1900$ MeV, where the cusp-like structure was seen for the photoproduction of $K^+\Sigma^0$ in a previous measurement at the BGOOD ([30]); it is likely that the cusp is driven by the dynamically generated $K^+\Sigma(1385)$ bound state.

4.2 Molecular nature of the $K^+\Sigma(1385)$ bound state

As discussed previously in Section 4.1, the condition of minimal momentum transfer affords a molecular description for this bound state. As such, a basic one-pion exchange 'toy model' is proposed, where this molecular state is bound together by a Yukawa-like interaction, i.e. purely by the exchange of pions.

This pure pion exchange is modeled into a pion propagator which scales as the inverse square of the momentum (q) of the $\Sigma(1385)$ determined in the rest frame of the K^+ [38]:

$$P = \frac{1}{(m_\pi^2 + q^2)} \tag{4.2}$$

For the purpose of calculating this propagator, initially a uniform distribution of beam energies from 1200 to 2200 MeV, and over angular ranges $\phi = (0, 2\pi)$, $\cos\theta^{K^+}_{\mathrm{CM}} = (0.9, 1.0)$ is generated. The distribution of four momentum of the incoming beam is then calculated from beam energy values sampled from this distribution. Further, the $\Sigma(1385)$ mass is sampled from a Breit Wigner distribution with the peak and decay width set according to the PDG values. The K^+ and π^0 masses are fixed to their nominal values. Subsequently, the four momenta of the K^+, $\Sigma(1385)$, the relative momenta and the pion propagator (P) are calculated using these values.

The two dimensional distribution of the events with respect to the relative momentum (in the K^+ rest frame), q and the center of mass energy, W is shown in Fig. 4.2(a). The histogram of the pion propagator squared, calculated from the values of q (and additionally multipled by the probability distribution of the events wrt. center of mass energy) can be seen in Fig. 4.2(b). Comparing Figs. 4.2(a) and 4.2(b) it can

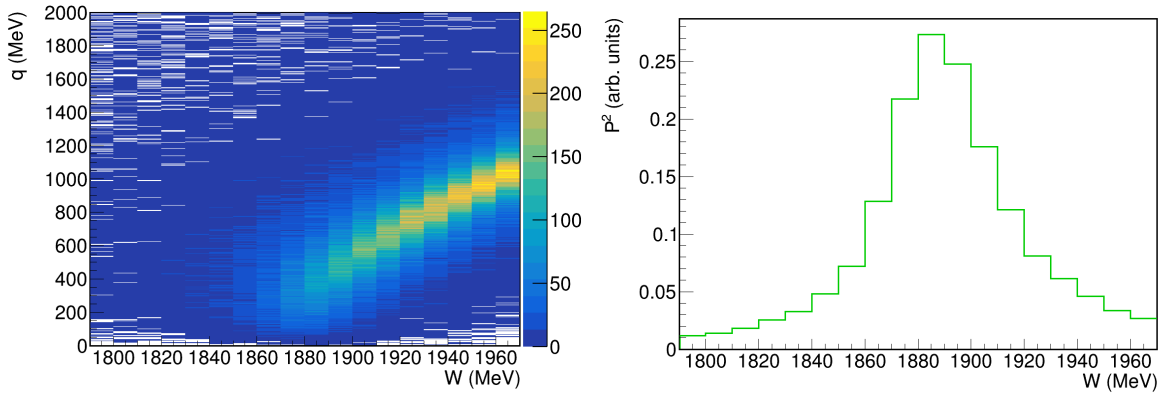

(a) (b)

Figure 4.2: Histograms of the (a) 2D distribution of the events wrt. relative momentum, q and the center of mass energy, W (b) 1D distribution of the pion propagator squared, P^2 vs. the center of mass energy W

be seen that at center of mass energy $W \approx 1885$ MeV, i.e. near the threshold, q is minimal. As such the pion propagator squared P^2, shows a peak as expected ($P^2 \propto 1/q^4$). Following this, at higher W, the P^2 decreases. One also finds that the slow rise in P^2 going from low energies till the threshold is caused by the finite width of $\Sigma(1385)$. Had the width of the Breit Wigner distribution for $\Sigma(1385)$ been set to zero, the P^2 would show a step-like jump from zero to a finite value, followed by the expected behaviour at the threshold and higher energies. It is to be noted that, for the purpose of comparison the calculated P^2 has been normalized to match the amplitude of the measured differential cross section for $\gamma p \rightarrow K^+\Sigma(1385)$ (in Fig. 4.1). Therefore, it is shown here in arbitrary units instead of MeV^{-4}.

It is clear that the 'toy model' i.e. this P^2 contribution, describes the shape of the measured differential cross section of $\gamma p \rightarrow K^+\Sigma(1385)$ quite well, especially around the threshold (as can be seen in Fig. 4.1). As such, it can be interpreted that close to the production threshold, this process is dominated by the t-channel exchange of a pion.

In order to build a model that additionally describes the amplitude of the measured differential cross section, the pion vertex factors and the matrix element for the process need to be calculated, which is beyond the scope of this thesis.

4.3 Comparison with the CLAS dataset

One of the previous measurements of the differential cross section for the process $\gamma p \rightarrow K^+\Sigma(1385)$ was taken by the CLAS collaboration [42]. This was however taken for more backward angles ($\cos\theta^{K^+}_{\mathrm{CM}} \in [-0.85, 0.84]$) and from energies above the $K^+\Sigma(1385)$ threshold, starting only from $W = 2000$ MeV. Also, the energy bins are 100 MeV wide, which is quite broad compared to the energy resolution for the present data. However, the statistical uncertainty on the values of $d\sigma/d\Omega$ measured by the CLAS is much lower than the present results. It is important to highlight that the current data in this thesis is the only differential cross section measurement taken around the threshold region and at the most forward angle, for this process. The current measurement of $d\sigma/d\Omega$ is compared with the CLAS dataset (at $\cos\theta^{K^+}_{\mathrm{CM}} = 0.84$) in Fig. 4.3. As the CLAS data starts at energies much above the region where this peaking behaviour occurs, one finds only a gentle decrease in the differential cross section at

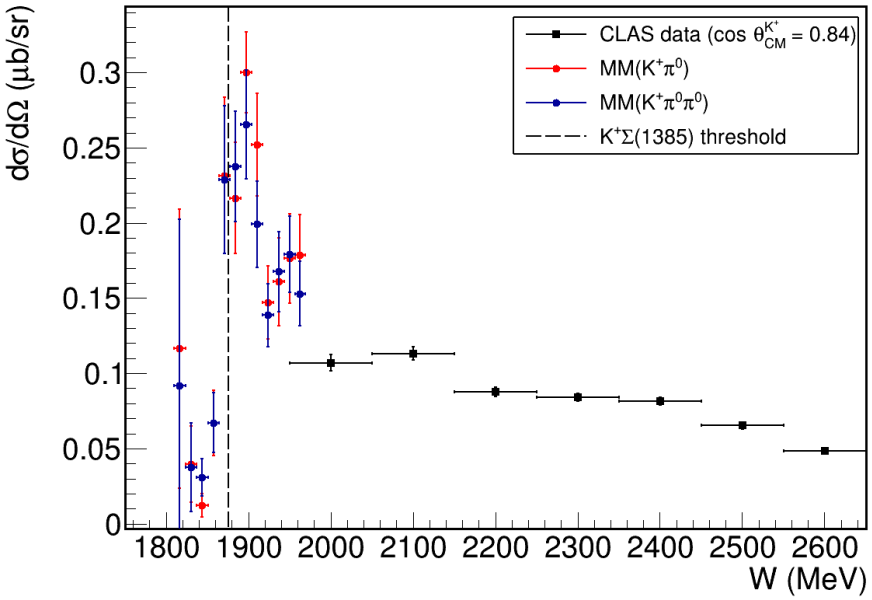

Figure 4.3: Comparison of measured differential cross section for the process $\gamma p \rightarrow K^+\Sigma(1385)$ (using the two missing mas techniques) with data obtained by the CLAS collaboration. The $K^+\Sigma(1385)$ nominal threshold is again indicated by the black dashed line.

higher energies, devoid of any interesting features. Following the general trend of decreasing $d\sigma/d\Omega$ at energies beyond $W \approx 1950$ MeV, it is plausible that there is a smooth continuity between the current measurement and the CLAS data.

CHAPTER 5

Summary and Outlook

While the present quark model describes the spectrum of ground state hadrons and their corresponding low lying excitations sufficiently well, as mesons ($q\bar{q}$) and baryons (qqq); for excited hadrons a number of discrepancies exist between the results from the theory and experimental observations. Several multi-quark states have been proposed to explain these observations [35].

One such example is seen in the differential cross section for photoproduction of $K^+\Sigma^0$ previously measured at the BGOOD experiment. It shows a peak like structure followed by a significant decrease around $W = 1900$ MeV (at very forward angles). Among a number of possible explanations, it was proposed [30] that this 'cusp' could potentially be driven by a bound state of the $K^+\Sigma(1385)$ with a mass of 1872.6 MeV and quantum numbers $J^P = (3/2)^-$ ([31]). If this turns out to be the case, then an interesting parallel between this proposed state in the strange quark sector and the $P_c(4380)$ state in the charm sector identified at the LHCb, could be established. In light of these results, a precise measurement near threshold and at forward K^+ angles for $\gamma p \rightarrow K^+\Sigma(1385)$ was considered essential to shed light on the reaction mechanism. As such, this work reports the differential cross section for the $\gamma p \rightarrow K^+\Sigma(1385)$ for the dominant decay channel $\Sigma(1385) \rightarrow \Lambda\pi^0$ at very forward angles ($\cos\theta^K_{CM} > 0.9$).

Initially, simulated datasets were generated for the $K^+\Sigma(1385)$ and the $K^+\Lambda(1405)$ final states. Following this, a number of preliminary and selection cuts were applied onto the experimental and simulated datasets, so as to retain only the events in the energy region and angular range to be studied. The selection cuts also involved identification cuts centered around the K^+ and π^0 mass, in order to identify the final decay products. A momentum and angle dependent correction factor was applied to the measured mass in the forward spectrometer. In order to extract the $K^+\Sigma(1385)$ events in the data, the missing mass from the $K^+\pi^0\pi^0$ and the $K^+\pi^0$ system were studied. The experimental data for these two missing mass distributions was fitted with simulated datasets for the $K^+\Sigma(1385)$ and $K^+\Lambda(1405)$ along with a background dataset (corresponding to π^+ misidentified as K^+). These fits were made for projections of the missing mass distributions, corresponding to each tagger energy bin. As such an energy dependent distribution of the yield was obtained. In addition to the yield, the measured flux distribution, the reconstruction efficiency, target area density and the solid angle were put together to arrive at the differential cross section for the process: $\gamma p \rightarrow K^+\Sigma(1385)$. Finally the systematic uncertainties were also computed. These involved reaction independent sources of uncertainty; and a fitting uncertainty. The latter was estimated by taking the ratio of the differential cross sections obtained using the two missing mass techniques and then making a constant line fit to it. An overall systematic

uncertainty of 11.5 % was achieved.

It is found that the measured differential cross section shows a pronounced rise (about three times) from center of mass energy of 1858 MeV till 1871 MeV, followed by a peak at 1898 MeV. This is a very interesting result as the peak appears close to the $K^+\Sigma(1385)$ threshold (W = 1876 MeV) and also near the predicted mass of the $K^+\Sigma(1385)$ bound state (W = 1872.6 MeV) which was suggested by *Huang et.al* ([31]). Furthermore, the cusp-like structure in the differential cross section of $\gamma p \rightarrow K^+\Sigma^0$ was also seen just at this peak (around 1900 MeV), lending credence to the suggestion that the $K^+\Sigma(1385)$ bound state may play a dominant role in causing the cusp effect seen in $K^+\Sigma^0$ photoproduction.

Emphasis is laid on the fact that at the $K^+\Sigma(1385)$ threshold and for K^+ going at very forward angles, the momentum transfer to the $\Sigma(1385)$ is minimal. Equivalently this is seen as a small relative momentum between the $\Sigma(1385)$ and K^+ in the rest frame of the K^+. Such conditions make it plausible for this bound state to exist. Therefore, the peak like structure seen for the differential cross section for $\gamma p \rightarrow K^+\Sigma(1385)$ near the threshold is interpreted as the signature of a $K^+\Sigma(1385)$ bound state. This is corroborated by a one pion exchange 'toy model' which involves a pion propagator, in turn dependent on the momentum of the $\Sigma(1385)$ in the K^+ rest frame. This 'toy model' replicates the shape of the measured differential cross section, indicating that this proposed $K^+\Sigma(1385)$ molecular state may be held together predominantly (especially around the threshold) by the exchange of pions, as is the case for a deuteron.

Finally, a comparison of the current data is made with an earlier measurement by the CLAS collaboration, of the differential photoproduction cross section for the same process. Putting the two datasets together, a general decrease in $d\sigma/d\Omega$ beyond 1950 MeV could be established. It is however noted that the CLAS data starts only at energies above the threshold and is in a more backward angular regime with much larger energy bins, therefore there isn't much overlap between the CLAS data and the current measurement. This comparison however highlights the significance of the current result as the only measurement carried out so far for differential cross section of $\gamma p \rightarrow K^+\Sigma(1385)$, at energies around the threshold and at the most forward K^+ angles.

As a future outlook, the differential cross section for this process may be measured for center of mass energies beyond 2000 MeV such that a better comparison with the CLAS dataset can be carried out. This would however involve the challenge of separating out background from the $K^{*+}\Sigma^0$ and $K^{*+}\Lambda^0$ which would have the exact same final decay products as the $K^+\Lambda(1405)$ and $K^+\Sigma(1385)$ respectively. It would also be interesting to use a phenomenological approach to investigate the structure of the $K^+\Sigma(1385)$ bound state. To this end, a form factor of the dipole type may be employed, with a cutoff parameter whose value would be determined by making fits of the calculated differential cross section to this measured data, as done for the CLAS data in the work of *J. He* [43]. The form factor can then be differentiated at zero momentum transfer, thereby giving an estimate of the root mean square radius and thereby the spatial extent of this bound state. All these ideas are however beyond the scope of the present study and will hopefully be pursued in a more expansive work.

APPENDIX A

Appendix

A.1 Missing mass distributions for the background and $\gamma p \rightarrow K^+\Lambda(1405)$ simulated data

The missing mass distributions that were not shown in Sec. 3.4.1 are shown here.

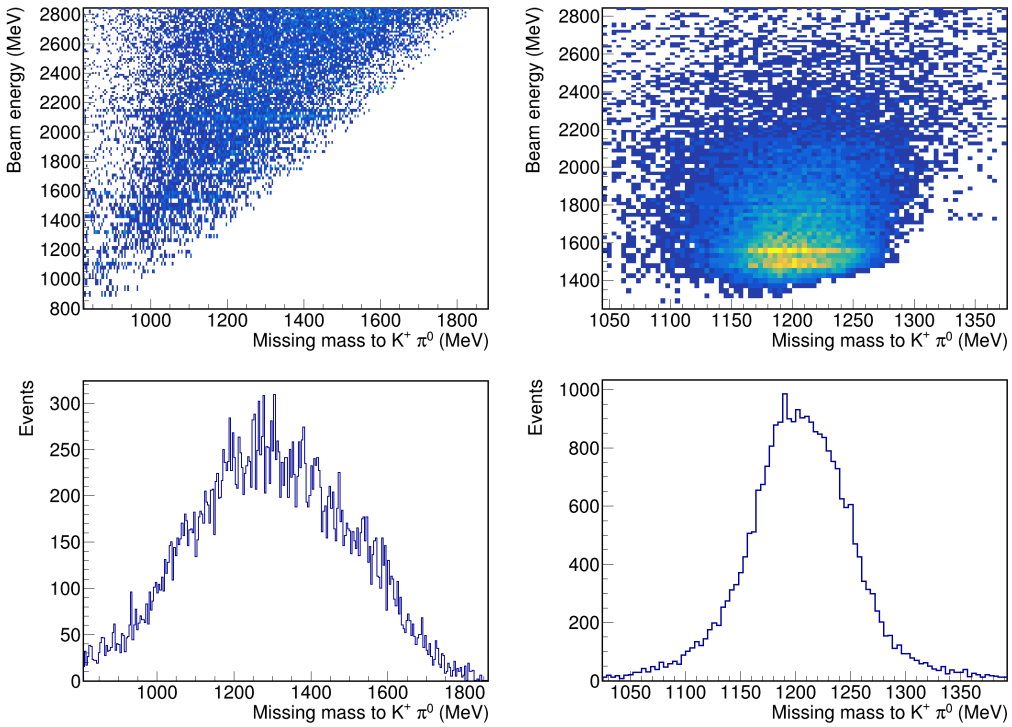

(a) Background data

(b) Simulated data for $\gamma p \rightarrow K^+\Lambda(1405)$

Figure A.1: 2D distributions of the beam energy v/s the missing mass to $K^+\pi^0$ and their projections (integrated over all beam energies) for background data and sim. $\gamma p \rightarrow K^+\Lambda(1405)$ data. The scaling of the axes is different in both the datasets so as to display most of the distribution of the events.

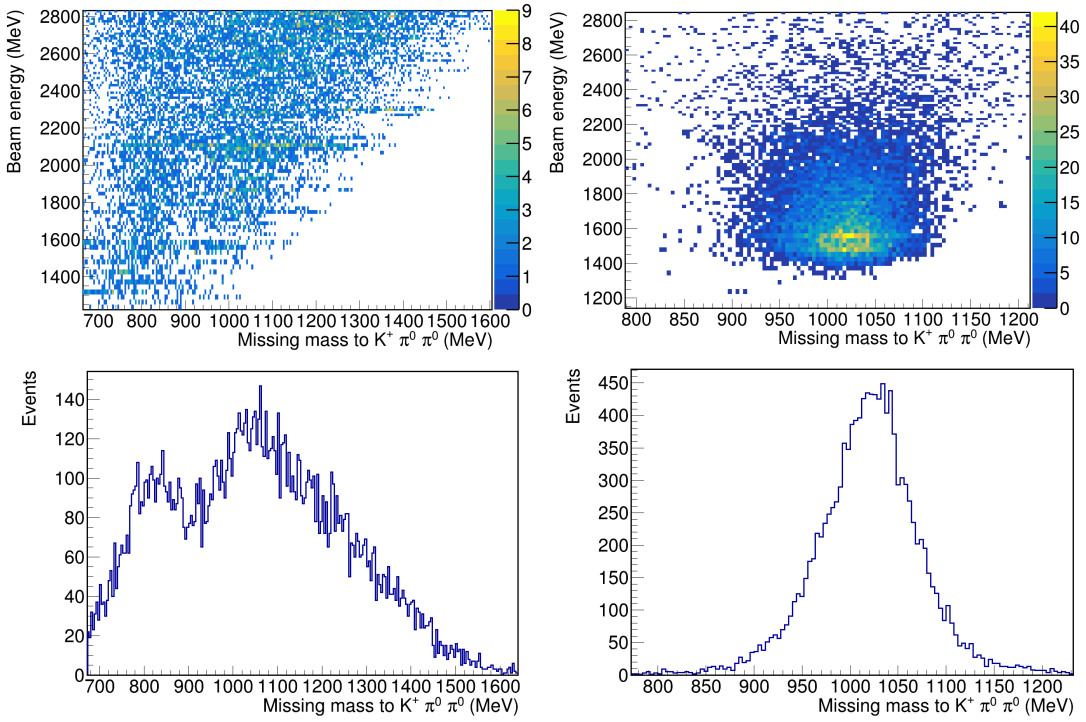

(a) Background data

(b) Simulated data for $\gamma p \rightarrow K^{+}\Lambda(1405)$

Figure A.2: 2D distributions of the beam energy v/s the missing mass to $K^{+}\pi^{0}\pi^{0}$ and their projections (integrated over all beam energies) for background data and sim. $\gamma p \rightarrow K^{+}\Lambda(1405)$ data.

Bibliography

[1] S. Manzoni, "The Standard Model and the Higgs Boson",
Physics with Photons Using the ATLAS Run 2 Data: Calibration and Identification, Measurement of the Higgs Boson Mass and Search for Supersymmetry in Di-Photon Final State,
Cham: Springer International Publishing, 2019 9, ISBN: 978-3-030-24370-8,
URL: https://doi.org/10.1007/978-3-030-24370-8_2.

[2] P. Aurenche, *The Standard Model of particle physics*, 1997, arXiv: hep-ph/9712342 [hep-ph].

[3] M. Thomson, *Modern Particle Physics*, Cambridge University Press, 2013.

[4] A. Tarek Abouelfadl Mohamed, "The Standard Model of Particle Physics",
Measurement of Higgs Boson Production Cross Sections in the Diphoton Channel: with the full ATLAS Run-2 Data and Constraints on Anomalous Higgs Boson Interactions,
Cham: Springer International Publishing, 2020 3, ISBN: 978-3-030-59516-6,
URL: https://doi.org/10.1007/978-3-030-59516-6_1.

[5] M. Gell-Mann, *Symmetries of Baryons and Mesons*, Phys. Rev. **125** (3 1962) 1067,
URL: https://link.aps.org/doi/10.1103/PhysRev.125.1067.

[6] F. Gross et al., *50 Years of quantum chromodynamics: Introduction and Review*,
The European Physical Journal C **83** (2023), ISSN: 1434-6052,
URL: http://dx.doi.org/10.1140/epjc/s10052-023-11949-2.

[7] P. D. Group et al., *Review of Particle Physics*,
Progress of Theoretical and Experimental Physics **2022** (2022) 083C01, ISSN: 2050-3911,
eprint: https://academic.oup.com/ptep/article-pdf/2022/8/083C01/49175539/ptac097.pdf,
URL: https://doi.org/10.1093/ptep/ptac097.

[8] C. Patrignani et al., *Review of Particle Physics, 2016-2017*, Chin. Phys. C **40** (2016) 100001,
URL: https://cds.cern.ch/record/2241948.

[9] T. Kawanai and S. Sasaki,
Interquark potential for the charmonium system with almost physical quark masses, Progress in Particle and Nuclear Physics **67** (2012) 130, From Quarks and Gluons to Hadrons and Nuclei,
ISSN: 0146-6410,
URL: https://www.sciencedirect.com/science/article/pii/S0146641011001232.

[10] H. Suganuma, "Quantum Chromodynamics, Quark Confinement, and Chiral Symmetry Breaking: A Bridge Between Elementary Particle Physics and Nuclear Physics", *Handbook of Nuclear Physics*, ed. by I. Tanihata, H. Toki and T. Kajino, Singapore: Springer Nature Singapore, 2020 1, ISBN: 978-981-15-8818-1, URL: https://doi.org/10.1007/978-981-15-8818-1_22-1.

[11] G. Eichmann, *Low-energy QCD phenomenology*, Lecture notes, 2020, URL: http://cftp.ist.utl.pt/~gernot.eichmann/2020-QCDHP/QCD-quark-models.pdf.

[12] M. Gell-Mann, *A Schematic Model of Baryons and Mesons*, Phys. Lett. **8** (1964) 214.

[13] G. Zweig, *An SU_3 model for strong interaction symmetry and its breaking; Version 2*, (1964), URL: https://cds.cern.ch/record/570209.

[14] N. Brambilla et al., *The XYZ states: Experimental and theoretical status and perspectives*, Physics Reports **873** (2020) 1, The XYZ states: experimental and theoretical status and perspectives, ISSN: 0370-1573, URL: https://www.sciencedirect.com/science/article/pii/S0370157320301915.

[15] A. Ali, J. S. Lange and S. Stone, *Exotics: Heavy pentaquarks and tetraquarks*, Progress in Particle and Nuclear Physics **97** (2017) 123, ISSN: 0146-6410, URL: https://www.sciencedirect.com/science/article/pii/S0146641017300716.

[16] H.-X. Chen, W. Chen, R.-R. Dong and N. Su, *$X_0(2900)$ and $X_1(2900)$: Hadronic Molecules or Compact Tetraquarks*, Chinese Physics Letters **37**, 101201 (2020) 101201, URL: https://cpl.iphy.ac.cn/EN/abstract/article_105745.shtml.

[17] F.-K. Guo et al., *Hadronic molecules*, Reviews of Modern Physics **90** (2018), ISSN: 1539-0756, URL: http://dx.doi.org/10.1103/RevModPhys.90.015004.

[18] S. L. Olsen, T. Skwarnicki and D. Zieminska, *Nonstandard heavy mesons and baryons: Experimental evidence*, Rev. Mod. Phys. **90** (1 2018) 015003, URL: https://link.aps.org/doi/10.1103/RevModPhys.90.015003.

[19] Z. Xu, *Experimental Study of Exotic Hadrons at LHCb*, Presented 15 Jun 2021, Peking U., 2021, URL: https://cds.cern.ch/record/2804389.

[20] S. Dubynskiy and M. Voloshin, *Hadro-charmonium*, Physics Letters B **666** (2008) 344, ISSN: 0370-2693, URL: http://dx.doi.org/10.1016/j.physletb.2008.07.086.

[21] F.-K. Guo, X.-H. Liu and S. Sakai, *Threshold cusps and triangle singularities in hadronic reactions*, Progress in Particle and Nuclear Physics **112** (2020) 103757, ISSN: 0146-6410, URL: http://dx.doi.org/10.1016/j.ppnp.2020.103757.

[22] M. C. Gordillo, F. De Soto and J. Segovia, *Structure of the $X(3872)$ as explained by a diffusion Monte Carlo calculation*, Phys. Rev. D **104** (5 2021) 054036, URL: https://link.aps.org/doi/10.1103/PhysRevD.104.054036.

[23] M. Karliner, J. L. Rosner and T. Skwarnicki, *Multiquark States*, Annual Review of Nuclear and Particle Science **68** (2018) 17, eprint: https://doi.org/10.1146/annurev-nucl-101917-020902, URL: https://doi.org/10.1146/annurev-nucl-101917-020902.

[24] G. Mezzadri and S. Spataro, *XYZ states: An experimental point-of-view*, Reviews in Physics **8** (2022) 100070, ISSN: 2405-4283, URL: https://www.sciencedirect.com/science/article/pii/S2405428322000028.

[25] R. Aaij et al., *Observation of a $J/\psi\Lambda$ Resonance Consistent with a Strange Pentaquark Candidate in $B^- \to J/\psi\Lambda\overline{p}$ Decays*, Phys. Rev. Lett. **131** (3 2023) 031901, URL: https://link.aps.org/doi/10.1103/PhysRevLett.131.031901.

[26] R. Aaij et al., *Observation of a Narrow Pentaquark State, $P_c(4312)^+$, and of the Two-Peak Structure of the $P_c(4450)^+$*, Phys. Rev. Lett. **122** (22 2019) 222001, URL: https://link.aps.org/doi/10.1103/PhysRevLett.122.222001.

[27] A. Ramos and E. Oset, *The role of vector-baryon channels and resonances in the $\gamma p \to K^0\Sigma^+$ and $\gamma n \to K^0\Sigma^0$ reactions near the $K^*\Lambda$ threshold*, Physics Letters B **727** (2013) 287, ISSN: 0370-2693, URL: https://www.sciencedirect.com/science/article/pii/S0370269313008058.

[28] T. Jude et al., *The BGOOD experiment at ELSA Exotic structures in the strange quark sector?*, EPJ Web of Conferences **271** (2022).

[29] K. Kohl et al., *Measurement of the $\gamma n \to K^0\Sigma^0$ differential cross section over the K^* threshold*, Eur. Phys. J. A **59** (2023) 254, arXiv: 2108.13319 [nucl-ex].

[30] T. Jude et al., *Observation of a cusp-like structure in the $\gamma p \to K^+\Sigma^0$ cross section at forward angles and low momentum transfer*, Physics Letters B **820** (2021) 136559, ISSN: 0370-2693, URL: https://www.sciencedirect.com/science/article/pii/S0370269321004998.

[31] H. Huang, X. Zhu and J. Ping, *P_c-like pentaquarks in a hidden strange sector*, Phys. Rev. D **97** (9 2018) 094019, URL: https://link.aps.org/doi/10.1103/PhysRevD.97.094019.

[32] S. Alef et al., *The BGOOD experimental setup at ELSA*, The European Physical Journal A **56** (2020), ISSN: 1434-601X, URL: http://dx.doi.org/10.1140/epja/s10050-020-00107-x.

[33] Georg Scheluchin, $\Lambda(1405)$ *photoproduction with the BGO-OD experiment*, PhD thesis: Rheinische Friedrich-Wilhelms-Universität Bonn, 2020, URL: https://hdl.handle.net/20.500.11811/8373.

[34] António João Clara Figueiredo, *Coherent $\pi^0\eta$ photoproduction off the deuteron at the BGOOD experiment*, Master's thesis: Rheinische Friedrich-Wilhelms-Universität Bonn, 2023, URL: https://www.pi.uni-bonn.de/schmieden/medien/medien-ergebnisse/master_thesis.pdf.

[35] Katrin Kohl, *Measurement of the $\gamma n \to K^0\Sigma^0$ photoproduction at the BGOOD experiment and the relation to possible pentaquark states*,
PhD thesis: Rheinische Friedrich-Wilhelms-Universität Bonn, 2022,
URL: https://hdl.handle.net/20.500.11811/9736.

[36] Adrian Sonnenschein, *$a_0(980)$ photoproduction at the BGOOD experiment*,
Master's thesis: Rheinische Friedrich-Wilhelms-Universität Bonn, 2021,
URL: https://www.pi.uni-bonn.de/schmieden/medien/medien-ergebnisse/master_thesis_adrian_sonnenschein.pdf.

[37] Oliver Freyermuth, *Studies of ω Photoproduction off Proton at the BGO-OD Experiment*,
PhD thesis: Rheinische Friedrich-Wilhelms-Universität Bonn, 2017,
URL: https://hdl.handle.net/20.500.11811/7263.

[38] T. Jude, Personal communication, 2024.

[39] A. Lazzaro and L. Moneta,
MINUIT package parallelization and applications using the RooFit package,
Journal of Physics: Conference Series **219** (2010) 042044,
URL: https://dx.doi.org/10.1088/1742-6596/219/4/042044.

[40] Andreas Stirner, *Coherent multi-meson photoproduction off a deuteron*,
Master's thesis: Rheinische Friedrich-Wilhelms-Universität Bonn, 2021,
URL: https://www.pi.uni-bonn.de/schmieden/medien/medien-ergebnisse/masterarbeit_andreas_stirner.pdf.

[41] S. Alef et al., *$K^+\Lambda$ photoproduction at forward angles and low momentum transfer*,
The European Physical Journal A **57** (2021), ISSN: 1434-601X,
URL: http://dx.doi.org/10.1140/epja/s10050-021-00392-0.

[42] K. Moriya et al.,
Differential photoproduction cross sections of the $\Sigma^0(1385)$, $\Lambda(1405)$, and $\Lambda(1520)$,
Phys. Rev. C **88** (4 2013) 045201,
URL: https://link.aps.org/doi/10.1103/PhysRevC.88.045201.

[43] J. He, *$\Sigma(1385)$ photoproduction from the proton within a Regge-plus-resonance approach*,
Phys. Rev. C **89** (5 2014) 055204,
URL: https://link.aps.org/doi/10.1103/PhysRevC.89.055204.

List of Figures

List of Tables